Electronic Supplementary Material (ESI) for Journal of Materials Chemistry A.

Supporting Information

ZIRCONIUM-METAL-ORGANIC FRAMEWORK@ACTIVATED CARBON COMPOSITES FOR PREVENTION OF SECOND EMISSION OF NERVE AGENTS

Table of contents

S.1. General considerations.

S.1.1. Materials and reagents.

Chemical reagents and solvents were purchased at commercial sources and used without additional purification. Activated carbon spheres were obtained from Blücher®.

S.1.2. Physical and chemical methods of characterization.

Powder X-Ray diffraction (PXRD) data were obtained on a D2 PHASER Bruker diffractometer using Cu Kα radiation (λ= 1.5418 Å), collecting in the 5-35° 2θ range with steps of 0.02° and a time between each step of 0.5 s. Carbonaceous substrates were deposited in the hollow of a zero-background silicon sample holder. **Nitrogen adsorption isotherms** were measured at 77 K on a Micromeritics 3Flex volumetric instrument. Prior to measurement, spheres samples were heated at 423 K for 7 h and outgassed to 10^{-1} Pa in a Micromeritics SmartVacPrep Module. **X-ray photoelectron spectroscopy (XPS)** data were collected with a KRATOS AXIS ULTRA-DLD X-ray photoelectron spectrometer consisting of a double anode X-ray source (Mg/Al), an Al Kα monochromator (600 W), ion gun with integrated gas inlet (Ar) for stripping and analysis chamber with heating and cooling accessory was used. **Fourier Transform Infrared Spectroscopy (FTIR)** spectra were recorded on a THERMO NICOLET IR200 equipped with an ATR module. Carbonaceous substrates cannot be put directly into the FTIR. It is necessary to prepare a pill of this material. The preparation of the pill is made from the carbonaceous sample and potassium bromide (KBr) powder. For each measurement, 2 mg of the carbonaceous sample and 200 mg of KBr are weighed. This mixture is ground to a fine powder and pressed to form the pill. **Inductively coupled plasma - mass spectrometry (ICP-MS)** measurements for zirconium quantification onto the composites were obtained on a PERKIN-ELMER NexION 300D ICP-MS spectrometer. **Potentiometric titration** data was collected using a Titrando 905 automatic titrator (Metrohm) set at the mode to collect the equilibrium pH. 100 mg of each sample was dispersed in $NaNO_3$ (50 mL, 0.01 M) in a container maintained at 25 °C, equilibrated overnight and continuously saturated with N_2. Then, the pH was adjusted to 4 using 0.1 M HCl (for samples with an acidic nature) or pH 10 using 0.1 M NaOH (for samples with a basic nature). Next, either 0.1M NaOH or HCl was used as titrating agent with an experimental window of pH 4-10. Distribution acidity constants were obtained using Saieus_pK software. **Scanning Electron Microscopy and Energy-Dispersive X-Ray (SEM-EDX)** analysis were obtained on a Field Emission Scanning Electron Microscope (FESEM) SCIOS 2 FIB-SEM system. DIFP degradation experiments were followed in an Agilent 8860 **Gas Chromatograph**. This chromatograph has a 16 port autosampler, a HP-5 column (50 m length, 0.320 mm diameter and 1.05 µm thickness) and a FID detector. **^{1}H and ^{31}P Nuclear Magnetic Resonance Spectroscopy** data was recorded on a 400 MHz BRUKER Nanobay Avance III HD High Definition spectrometer. **Thermogravimetric Analysis (TGA)** were carried out in a METTLER-TOLEDO mod. TGA/DSC1 system under N_2 atmosphere using a 20ºC/min ramp temperature from room temperature to 950 ºC.

High Resolution-Powder X-Ray Diffraction (HR-PXRD) measurements were performed at the high resolution PXRD beamline (ID-22) [ref: J. Synchrotron Rad. (2023). 30, 1003-1012 https://doi.org/10.1107/S1600577523004915] at the European Synchrotron radiation facility (ESRF, Grenoble France, experiment number: ch-6718) [ref: Borrego Marín, E., Carmona Fernandez, F.J., Vismara, R. 2026: Unveiling the phosphate adsorption sites in a series of Zr-based MOFs by in situ HR-PXRD. DOI: 10.15151/ESRF-ES-1323886503]. The studied samples were gently ground and introduced into a 0.5 mm diameter borosilicate glass capillary. The capillary was first aligned and then the HR-PXRD data collected. To minimize preferred-orientation effects and obtain very accurate diffracted intensities, the capillary was spinned during data acquisition. The sample radiation damage was monitored and prevented by translating the capillary a total of 20 times during the whole experiment. Data were collected at room temperature, working at 35 keV (λ = 0.355 Å, calibrated with the Si NIST standard SRM 640c at room temperature) with a beam size of 1 mm (horizontal) by 0.9 mm (vertical) defined by water-cooled slits and monochromated with a cryogenically cooled Si 111 channel-cut crystal. A bank of nine detectors, each preceded by a Si 111 analyser crystal, was scanned vertically to measure the diffracted intensity. Le Bail refinements were carried out on the collected data to qualitative confirm the presence of UiO-66/UiO-66-NH_2 coating on the activated carbon spheres composites.

S.2. Synthesis of materials.

S.2.1. Synthesis of UiO-66 and UiO-66-NH_2

S. 2.1.1. Layer-by-Layer type synthesis

UiO-66-(NH_2) synthesis (materials will be named UiO-66(-NH_2) LBL) were carried out by using the same conditions as in layer-by-layer procedure (see S.2.4). For each product, we prepared two separate solutions of ligand and Zr cluster. Ligand solution was prepared by dissolving 750 mg (4.51 mmol) of 1,4-benzenedicarboxylic acid (H_2bdc) (for UiO-66 LBL) or 817,8 mg (4.51 mmol) of 2-ammino-1,4-benzenedicarboxylic acid (H_2bdc-NH_2) (for UiO-66-NH_2 LBL) in 100 mL of N,N-dimethylformamide (DMF). The $Zr_6O_6(OH)_6(AcO)_{12}$ cluster solution was prepared according to the procedure reported by Farha et al. In a round bottom flask it was added 710 µL of a $Zr(OPr)_4$/PrOH solution, 70 mL of DMF and 40 mL of acetic acid in a 100 mL. This mixture was heated at 130ºC without stirring for three hours, when a yellow-orange solution appeared.

Next, we mixed both ligand and cluster solution and heated at 130 ºC during 6 hours (same time as for the layer-by-layer synthesis, see S.2.4). A white and yellow powder appeared for UiO-66 LBL and UiO-66-NH_2 LBL products, respectively. Each material was filtered and washed with DMF by triplicate.

S. 2.1.2. Solvothermal synthesis

For UiO-66 solvothermal synthesis we mixed 1.29 g $ZrCl_4$ (5.55 mmol), 1.84 g bencene-1,4-dicarboxylic acid, 0.925 mL HCl and 37.5 mL DMF. This reaction mixture was heated at 220 ºC during 16h. Finally, the white solid was filtered, washed with DMF by triplicate, acetone and dried at room temperature during 24 hours.

For UiO-66-NH_2 solvothermal synthesis we mixed 1.29 g $ZrCl_4$ (5.55 mmol), 2.01 g bencene-2-amino-1,4-dicarboxylic acid, 0.925 mL HCl and 37.5 mL DMF. This reaction mixture was heated at 220 ºC during 16h. Finally, the yellow solid was filtered, washed with DMF by triplicate, acetone and dried at room temperature during 24 hours.

S.2.2. Oxidation of Blücher® spheres.

In this work, we carried out three different oxidation procedures for activated carbon spheres.

S.2.2.1. Oxidation of the spheres with H_2O_2.

We added 100 mL of H_2O_2 to 2.5 g of Blücher® activated carbon spheres. This suspension was kept for 1 h at room temperature (bubbling is observed). Then, the spheres were collected and washed several times with distilled water until the pH of the wash water remains constant. Finally, the spheres were dried in an oven for a couple of hours.

S.2.2.2. Oxidation of the spheres with HNO_3.

We added 100 mL of 65% pure HNO_3 to 2.5 g of Blücher® activated carbon spheres in a round bottom flask and refluxed at 80°C for 30 minutes. Then, the flask was allowed to cool to room temperature. The spheres were washed thoroughly in a Soxhlet to remove any remaining acid. The Soxhlet washing was done vigorously at 190 °C until the pH of the washing water stabilized. The spheres were collected and dried in an oven.

S.2.2.3. Oxidation of the spheres with $(NH_4)_2S_2O_8$.

We added 100 mL of a saturated solution of ammonium persulfate ($(NH_4)_2S_2O_8$) in 1M sulphuric acid to 2.5 g of Blücher® activated carbon spheres. The spheres were stirred in this solution for 10 hours. After this time, they were recovered and washed in the Soxhlet. Washing was carried out until the pH of the wash water was constant. The washed spheres were dried in an oven for a few hours.

S.2.3. Functionalization of AC spheres using urea and thiourea.

We prepared a mixture of 1.5 g of urea, 1.5 g of oxidized activated carbon spheres (AC(Y005)_H_2O_2, AC(Y005)_HNO_3 or AC(Y005)_$(NH_4)_2S_2O_8$) and a volume of water sufficient to dissolve urea. The mixture of the oxidized spheres and urea in water was sonicated for 1 hour and then the flask was transferred to the rotary evaporator to evaporate the solvent. In this way, the spheres were partially coated with a white solid.

Then, these impregnated spheres were subjected to a heat treatment. The samples were placed in a CARBOLITE quartz tube furnace, sealed with septums at both ends and connected to an external N_2 current. Prior to heat treatment, a N_2 steam was passed through the system for 5 minutes to generate an inert atmosphere in the system. The heat treatment consisted of a 10 ºC/min ramp-up to 450 ºC, was maintained at this temperature for 30 minutes, and ended up with a 10 ºC/min ramp-down. The spheres obtained were repeatedly washed with distilled H_2O until the pH of the wash water was constant.

The same experimental process was repeated to functionalize oxidized AC(Y005) spheres with thiourea.

S.2.4. Synthesis of MOF@AC composites.

S.2.4.1. Zirconium oxohydroxide cluster solution.

The $Zr_6O_6(OH)_6(AcO)_{12}$ cluster solution used was the same for the growth of UiO-66 and for UiO-66-NH_2. It was prepared according to the procedure reported by Farha et al.[1] In a round bottom flask it was added 710 µL of a $Zr(OPr)_4$/PrOH solution, 70 mL of DMF and 40 mL of acetic acid in a 100 mL. The mixture was heated at 130ºC without stirring for three hours, when a yellow-orange solution appeared.

S.2.4.2. Ligand solution.

In order to synthesize UiO-66, 1,4-benzenedicarboxylic acid (H_2bdc) solution was prepared by dissolving 750 mg (4.51 mmol) of H_2bdc in 100 mL of DMF. For the UiO-66-NH_2 synthesis, 2-ammino-1,4-benzenedicarboxylic acid (H_2bdc-NH_2) solution was prepared by dissolving 817,8 mg (4.51 mmol) of H_2bdc-NH_2 in 100 mL of DMF

S.2.4.3. Layer-by-Layer synthesis of Zr-MOFs@AC spheres composites.

1.5 g of the oxidized activated carbon spheres were immersed into the cluster solution at 130 °C for 15 minutes under gentle agitation. Then, the spheres were filtered, washed 3 times with DMF and dried under vacuum. Subsequently, they were immersed in the ligand solution (H_2bdc for UiO-66 or H_2bdc-NH_2 for UiO-66-NH_2 synthesis) and heated at 130 °C for 15 minutes under stirring. After this time, the spheres were filtered, washed 3 times with DMF and dried under vacuum. This process was repeated successively up to 12 cycles on each of the oxidized spheres (AC(Y00n)_HNO_3 , n=1-5). A cycle is considered when immersion in both cluster and ligand solutions has taken place.

S.3. DIFP catalytic tests.

S.3.1. Gas Chromatography studies.

Self-detoxification studies

We have proceeded to the catalytic degradation of diisopropylfluorophosphate (DIFP) as a model of nerve Chemical Warfare Agent (CWA) similarly to previous works by our group[2-4]. The degradation of DIFP was studied employing 40 mg of composite (UiO-66(-NH_2)@AC(Y00n)_HNO_3, n=1-5) or pristine spheres (AC(Y00n), n=1-5), 2 µL of H_2O, and 0.3 µL of DIFP (0.865 M) in a closed vial with a septum. The evolution of DIFP concentration was followed at room temperature during 24 h. In addition, a set of parallel experiments with different cycles were carried out in order to evaluate the progress of the detoxification reaction. When the catalytic test is finished, we carried out the extraction with 700 µL of $CHCl_3$ during 2 h. Afterwards, 0.3 µL of N,N-dimethylacetamide (DMA) was added as an internal standard before measurement by means of Gas Chromatography employing an Agilent 30 m-column (0.53 mm internal diameter) (Fig. 39). In addition, we studied the evolution of DIFP concentration against time using the conditions previously mentioned. We also carried out the extraction of DIFP with 700 µL $CHCl_3$ during 2 h and measured by means of Gas Chromatography Agilent 30 m-column using 0.3 µL of DMA as an internal standard (Fig. S40).

Catalyst reusability tests

Finally, we studied the possibility to reuse UiO-66(-NH_2)@AC(Y00n)_HNO_3 (n=4, 5) composites in more than one DIFP catalysis. Firstly, DIFP degradation was studied employing 40 mg (UiO-66(-NH_2)@AC(Y00n)_HNO_3, n=4, 5) of composite, 2 µL of H_2O, and 0.3 µL of DIFP (0.865 M) in a closed vial with a septum (1° pulse). The evolution of DIFP concentration was followed at room temperature after 24 h. After that, we introduced two additional pulses (one every

24 h) of DIFP (0.3 µL) in order to study the recyclability capacity of these materials. DIFP extraction was carried out with 700 µL $CHCl_3$ during 2 h and measured by means of Gas Chromatography Agilent 30 m-column using 0.3 µL of DMA as an internal standard.

Catalytic activity of MOF:AC spheres physical mixtures

For comparative reasons, we also studied the ability of a physical mixture of MOF-AC to degrade DIFP using the same conditions of the composites above mentioned. First, this physical mixture was prepared as a slurry by sonicating a suspension of UiO-66(-NH_2) with oxidized AC(Y00n)_HNO_3 (n = 4-5) in acetone for 15 minutes keeping the same MOF:AC ratio composition as in the synthesize composites. Then, the flask was transferred to the rotary evaporator to evaporate the acetone and the mixture was dried at room temperature. DIFP degradation was studied employing 40 mg of the physical mixture (UiO-66+AC(Y004), UiO-66+AC(Y005), UiO-66-NH_2+AC(Y004) and UiO-66-NH_2+AC(Y005)), 2 µL of H_2O, and 0.3 µL of DIFP (0.865 M) in a closed vial with a septum. The modification of DIFP concentration was followed at room temperature at 24 h. In order to know the composition of the adsorbate phase, we carried out the extraction with 700 µL of $CHCl_3$ during 2 h, added 0.3 µL of N,N-dimethylacetamide (DMA) as an internal standard and measured by means of Gas Chromatography employing an Agilent 30 m-column (0.53 mm internal diameter).

S.3.2. Nuclear Magnetic Resonance studies.

In order to determinate the presence of degradation products, we carried out the extraction with 700 µL of $CDCl_3$ and $NaHCO_3$ solution (10.2 mM) in D_2O after each reaction and measured by ^{1}H-NMR and ^{31}P-NMR (Fig. S42-45).

S.4. DIP solid-liquid adsorption isotherms.

We evaluated the solid-liquid adsorption capacity of AC(Y00n) and UiO-66(-NH_2) LBL (n=4, 5) materials towards DIFP degradation product, diisopropylphosphate (DIP). We suspended 2 mg of the different materials and equilibrated the material during 24 h at 25 ºC with D_2O solutions of DIP (0.05-0.5 mM, 1 mL). After this period, we centrifuged the sample, added dimethylphosphate (DMP) as an internal standard and quantified the DIP concentration by ^{1}H and ^{31}P NMR.

The adsorption capacity of each material was calculated as follows:

$$q = \frac{Co - Ce}{C\,MOF}$$

q = adsorption capacity (mol·mol^{-1})
C_0 = initial concentration of diisopropylphosphate (mM)
C_e = concentration of diisopropylphosphate after 24 h of adsorption
C_{MOF} = concentration of material in the aqueous suspension

Finally, the experimental data were fitted to adsorption Langmuir equation:

$$q_e = \frac{qmax \cdot K \cdot Ce}{1 + K \cdot Ce}$$

q_e = adsorption capacity (mol·mol-1) after 24 h of adsorption
q_{max} = maximum adsorption capacity (mol·mol^{-1})
K = Langmuir constant of adsorption (L·mol^{-1})

S.5. Inhibitory effect of DIP on DIFP degradation.

In order to understand the DIFP degradation mechanism of UiO-66(-NH$_2$)@AC(Y00n)_HNO$_3$ (n=4, 5) hybrid materials we studied the simultaneous DIP adsorption and DIFP catalytic degradation. First, we added 0.3 µL of diisopropylphosphate (DIP) into 40 mg of each material: AC(Y00n)_HNO$_3$, UiO-66(-NH$_2$) LBL and UiO-66(-NH$_2$)@AC(Y00n)_HNO$_3$ (n=4, 5). After 10 minutes, we added 0.3 µL of diisopropylfluorophosphate (DIFP), 2 µL of H_2O and stirred during 24 hours in a closed vial with a septum. Then, we carried out the extraction with 700 µL of $CHCl_3$ during 2 hours and recollected the supernatant. Finally, we added 0.3 µL of DMA to the supernatant as an internal standard before measurement by means of Gas Chromatography.

Figures

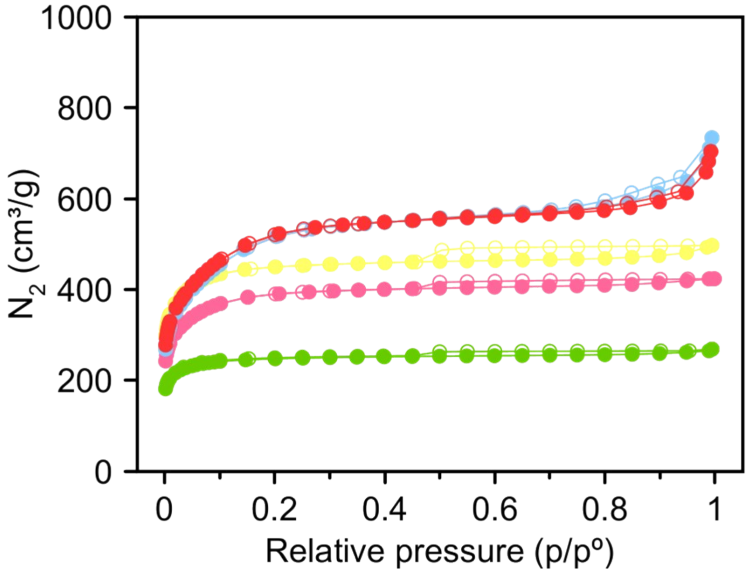

Figure S1. Nitrogen adsorption isotherms of pristine activated carbon spheres AC(Y001) (yellow curve), AC(Y002) (green curve), AC(Y003) (pink curve), AC(Y004) (blue curve) and AC(Y005) (red curve).

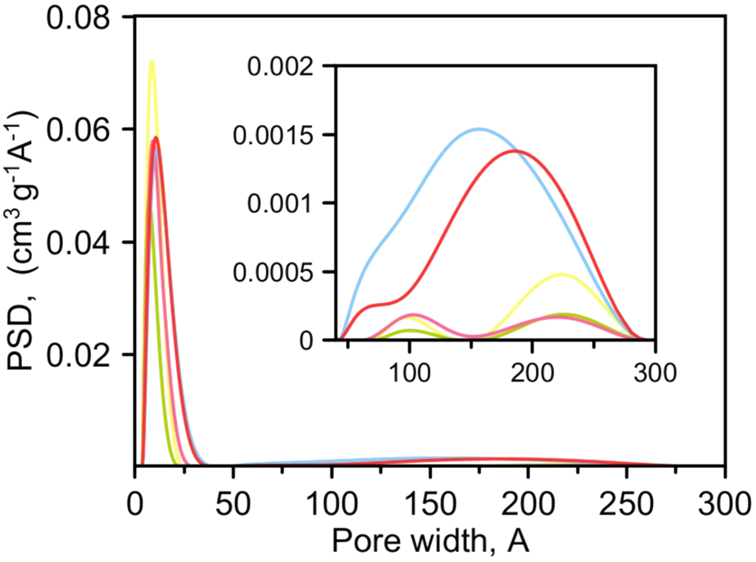

Figure S2. Pore size distribution of pristine activated carbon spheres AC(Y001) (yellow curve), AC(Y002) (green curve), AC(Y003) (pink curve), AC(Y004) (blue curve) and AC(Y005) (red curve) (inset: range extension between 40-300 Å).

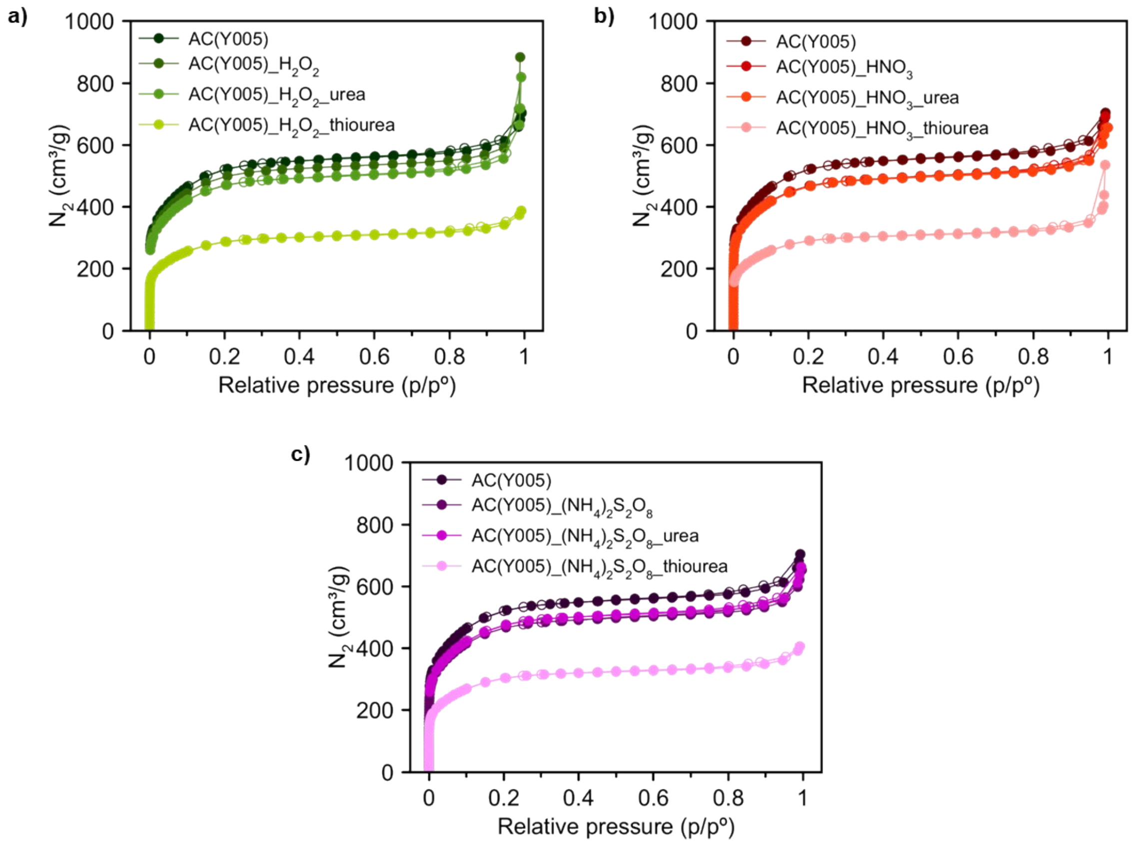

Figure S3. Nitrogen adsorption isotherms at 77 K for activated carbon sphere AC(Y005) oxidized with (a) H_2O_2, (b) HNO_3 and (c) $(NH_4)_2S_2O_8$, and followed by subsequent treatment with urea and thiourea.

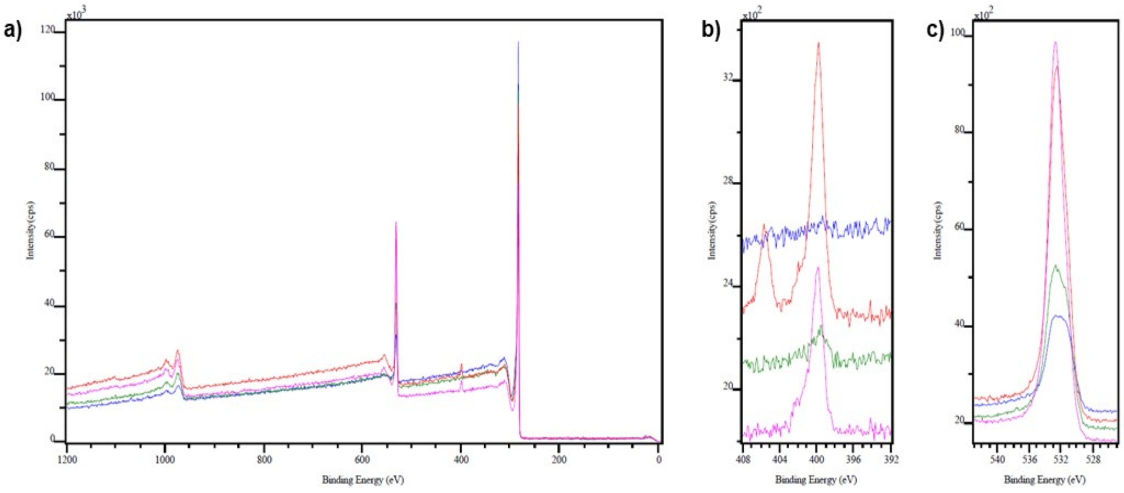

Figure S4. (a) Comparative XPS spectra and elemental quantification of (b) nitrogen and (c) oxygen for activated carbon sphere AC(Y005) before (blue curve), and after oxidation with H_2O_2 (green curve), HNO_3 (red curve) and $(NH_4)_2S_2O_8$ (purple curve).

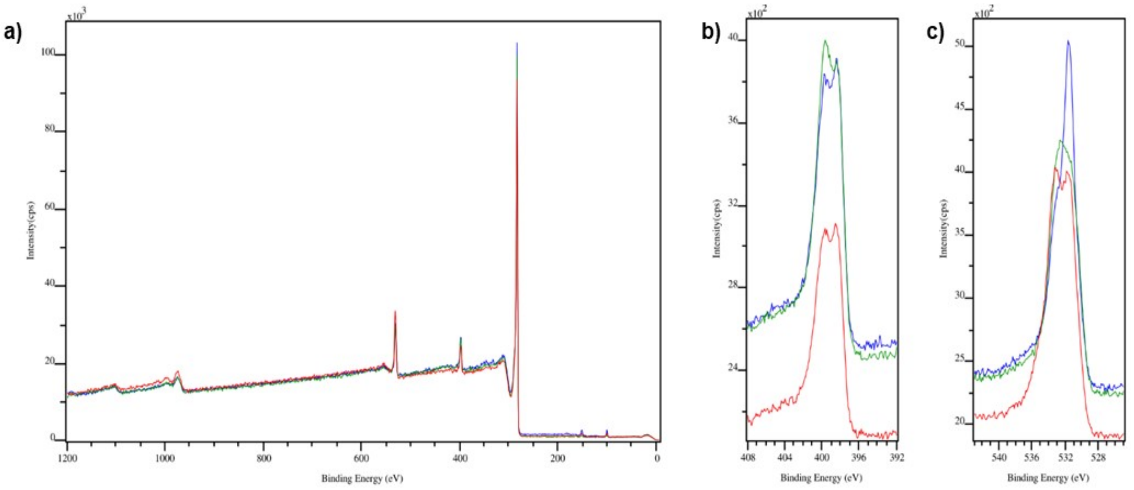

Figure S5. (a) Comparative XPS spectra and elemental quantification of (b) nitrogen and (c) oxygen for the activated carbon spheres AC(Y005) oxidized with H_2O_2 (blue), HNO_3 (green) and $(NH_4)_2S_2O_8$ (red) followed by subsequent treatment with urea.

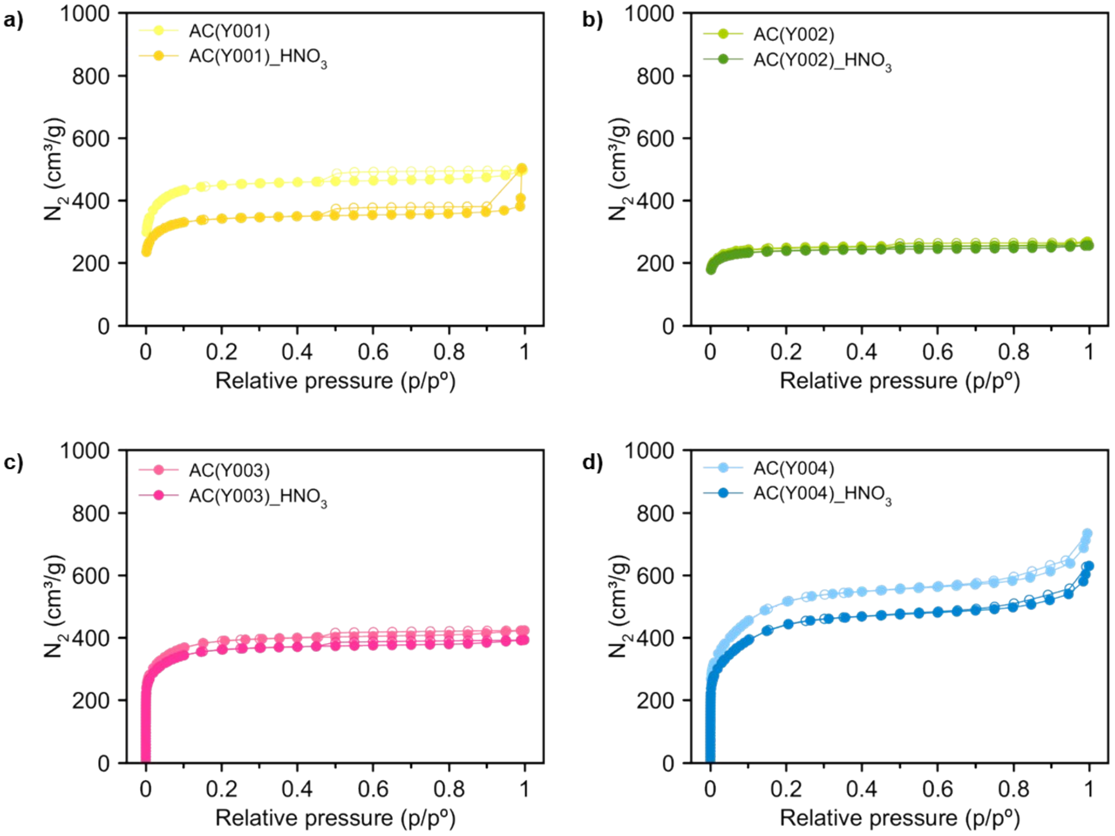

Figure S6. Nitrogen adsorption isotherms at 77K of activated carbon spheres before and after oxidation with HNO_3: (a) AC(Y001), (b) AC(Y002), (c) AC(Y003), (d) AC(Y004).

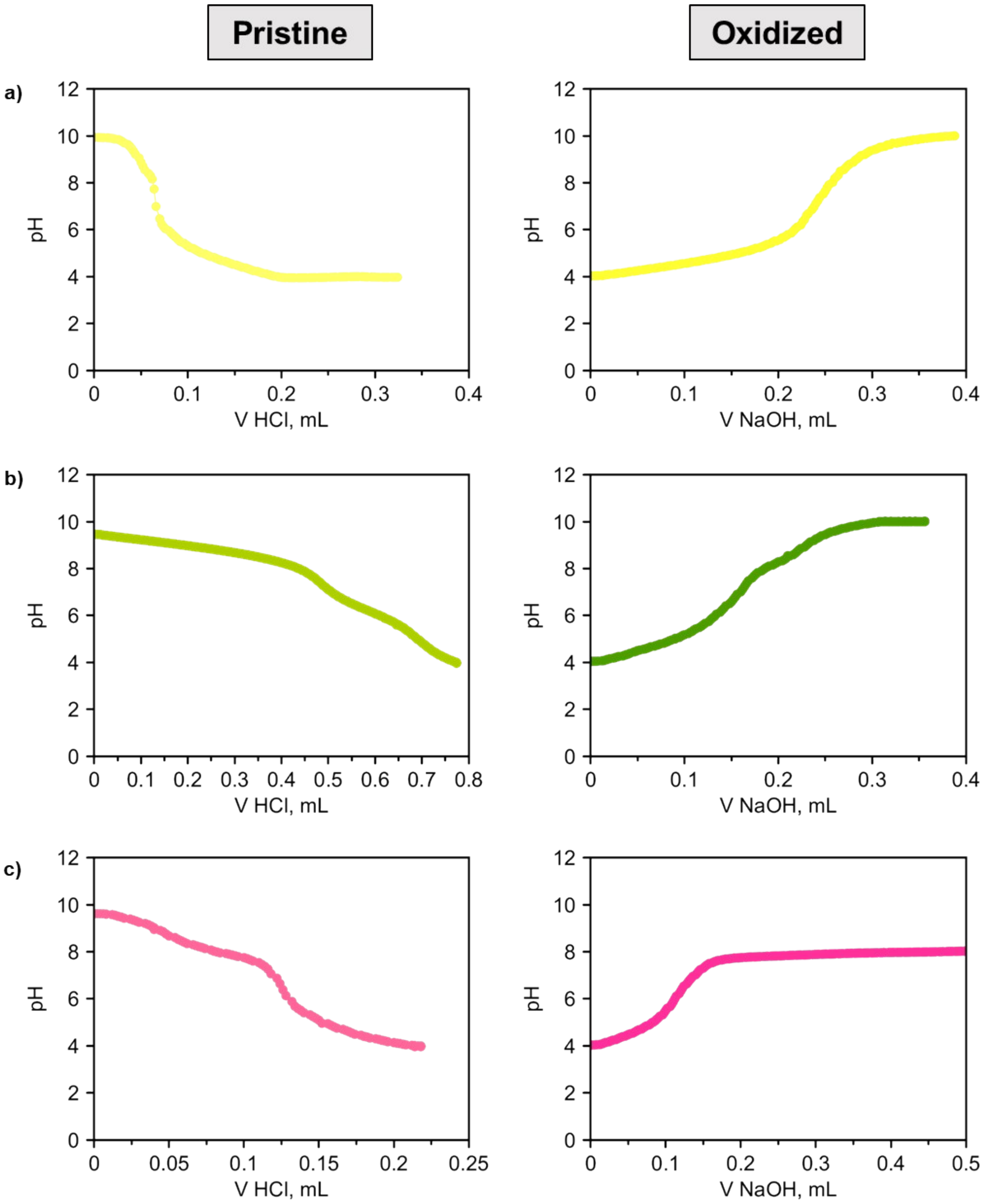

Figure S7. Acid-base titration curves for pristine and HNO_3 oxidized activated carbon spheres (a) AC(Y001), (b) AC(Y002) and (c) AC(Y003).

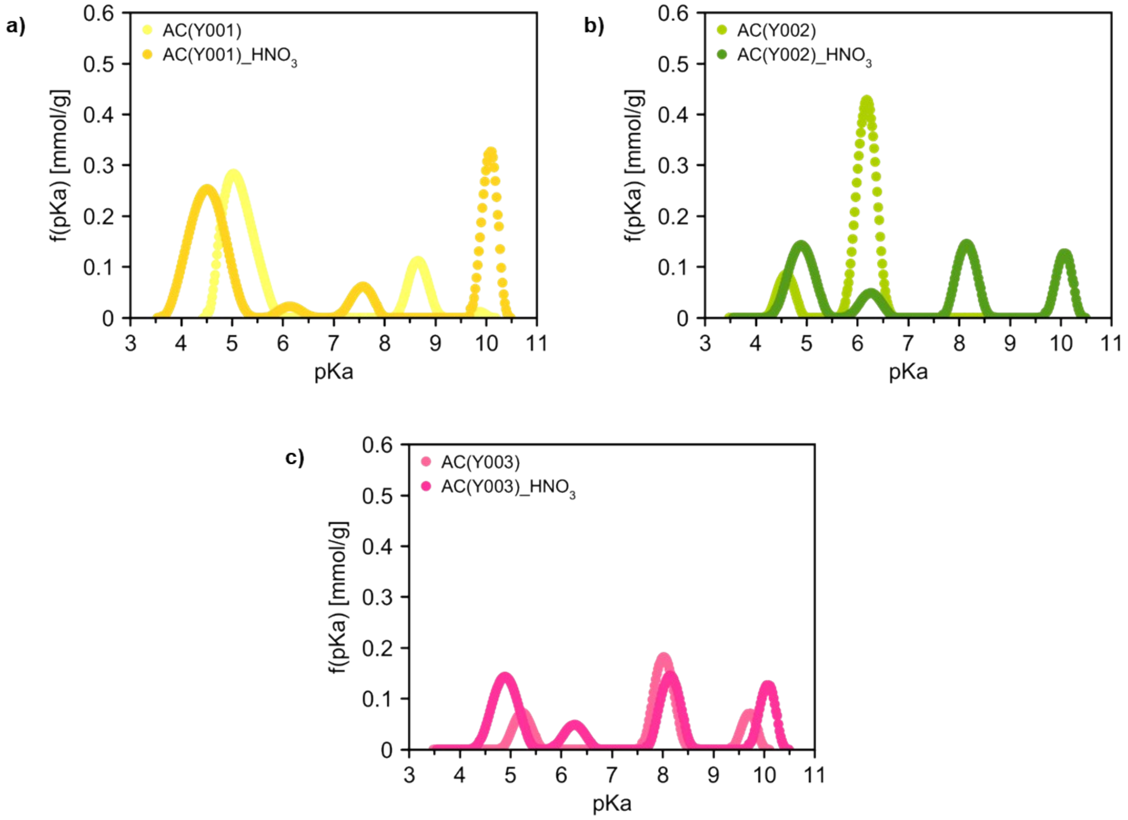

Figure S8. Distribution of acidity constants for pristine and HNO_3 oxidized activated carbon spheres (a) AC(Y001), (b) AC(Y002) and (c) AC(Y003).

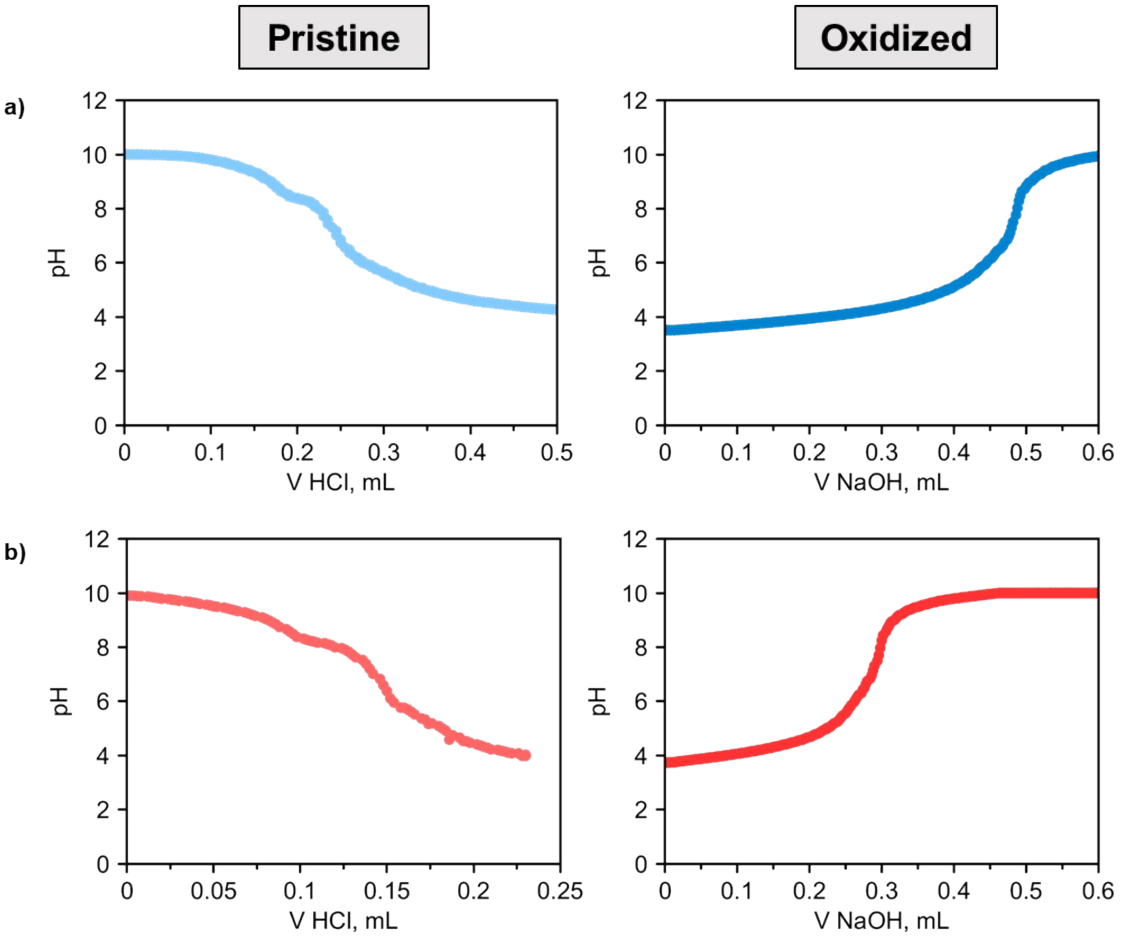

Figure S9. Acid-base titration curves for pristine and HNO_3 oxidized activated carbon spheres (a) AC(Y004) and (b) AC(Y005).

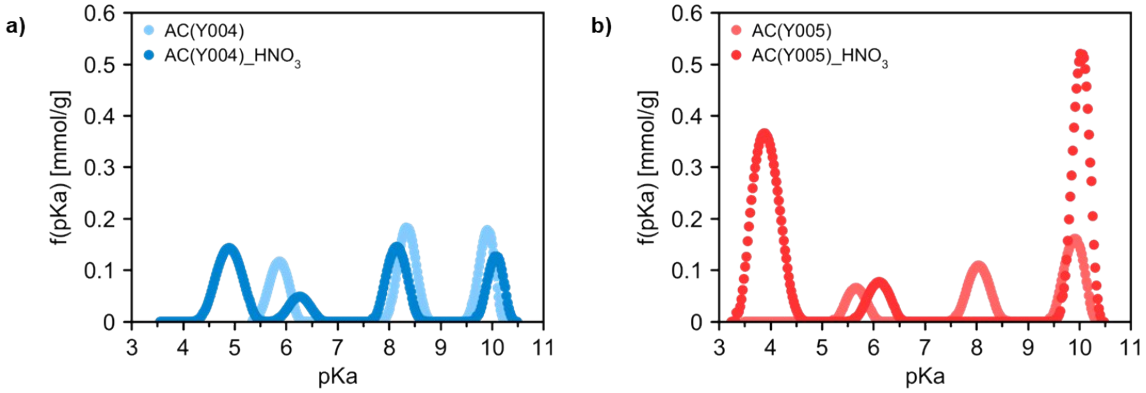

Figure S10. Distribution of acidity constants for pristine and HNO_3 oxidized activated carbon spheres (a) AC(Y004) and (b) AC(Y005).

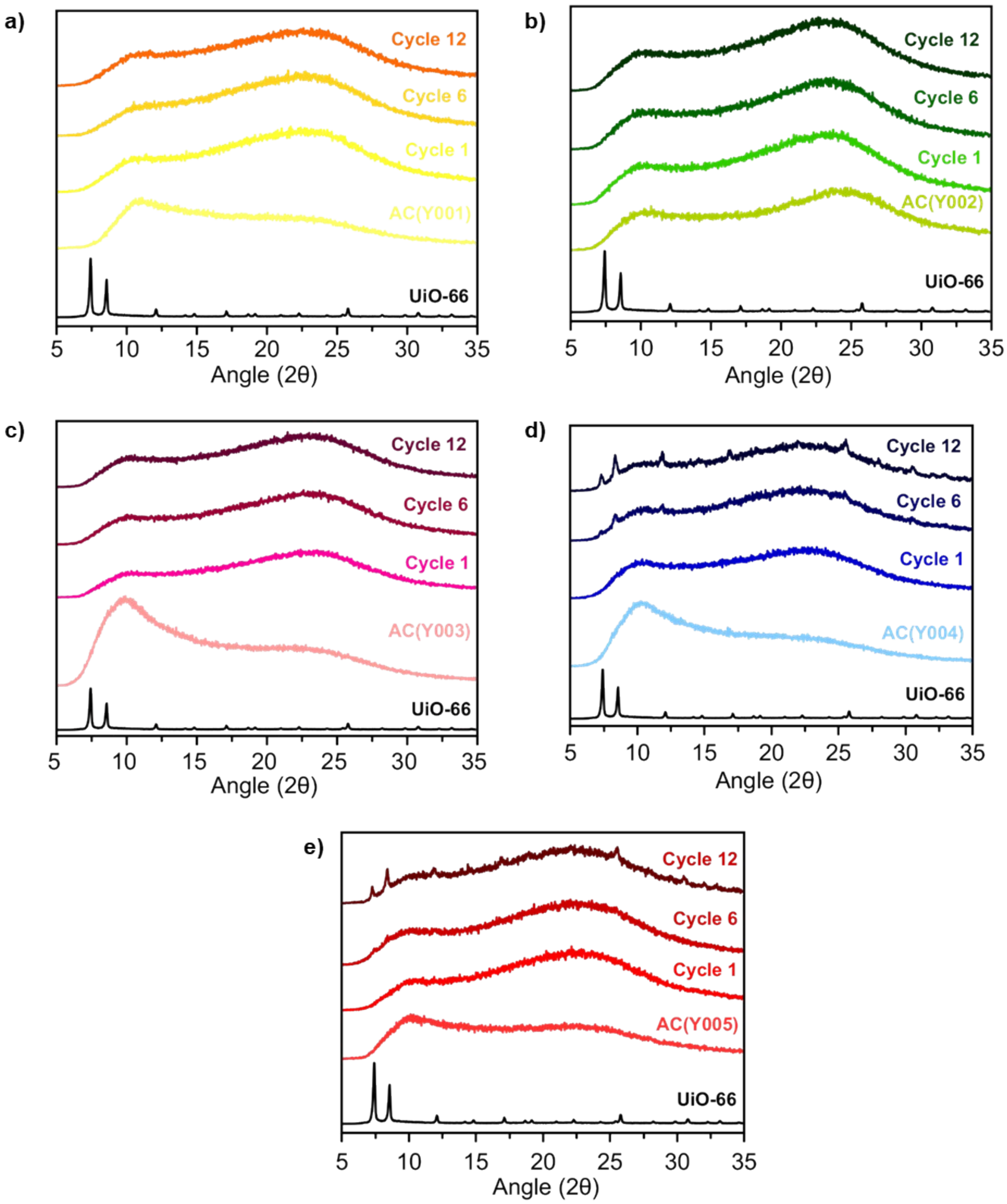

Figure S11. Follow-up of the layer-by-layer growth of UiO-66 thin films on the oxidized activated carbon spheres (a) AC(Y001), (b) AC(Y002), (c) AC(Y003), (d) AC(Y004) and (e) AC(Y005) by powder X-ray diffraction. The simulated UiO-66 pattern is shown in black.

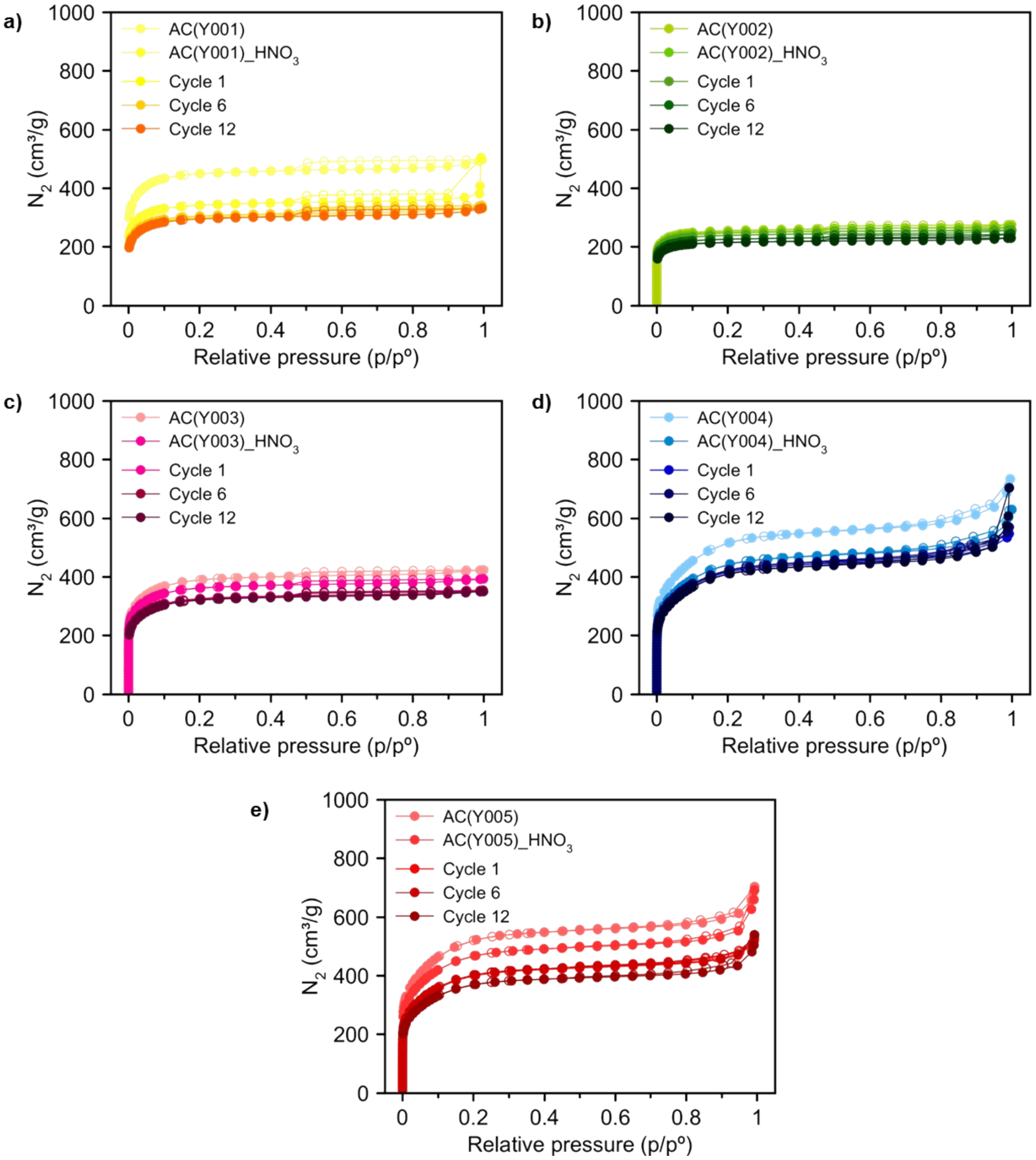

Figure S12. Follow-up of the layer-by-layer growth of UiO-66 thin films on the oxidized activated carbon spheres (a) AC(Y001), (b) AC(Y002), (c) AC(Y003), (d) AC(Y004) and (e) AC(Y005) by nitrogen adsorption isotherms at 77K.

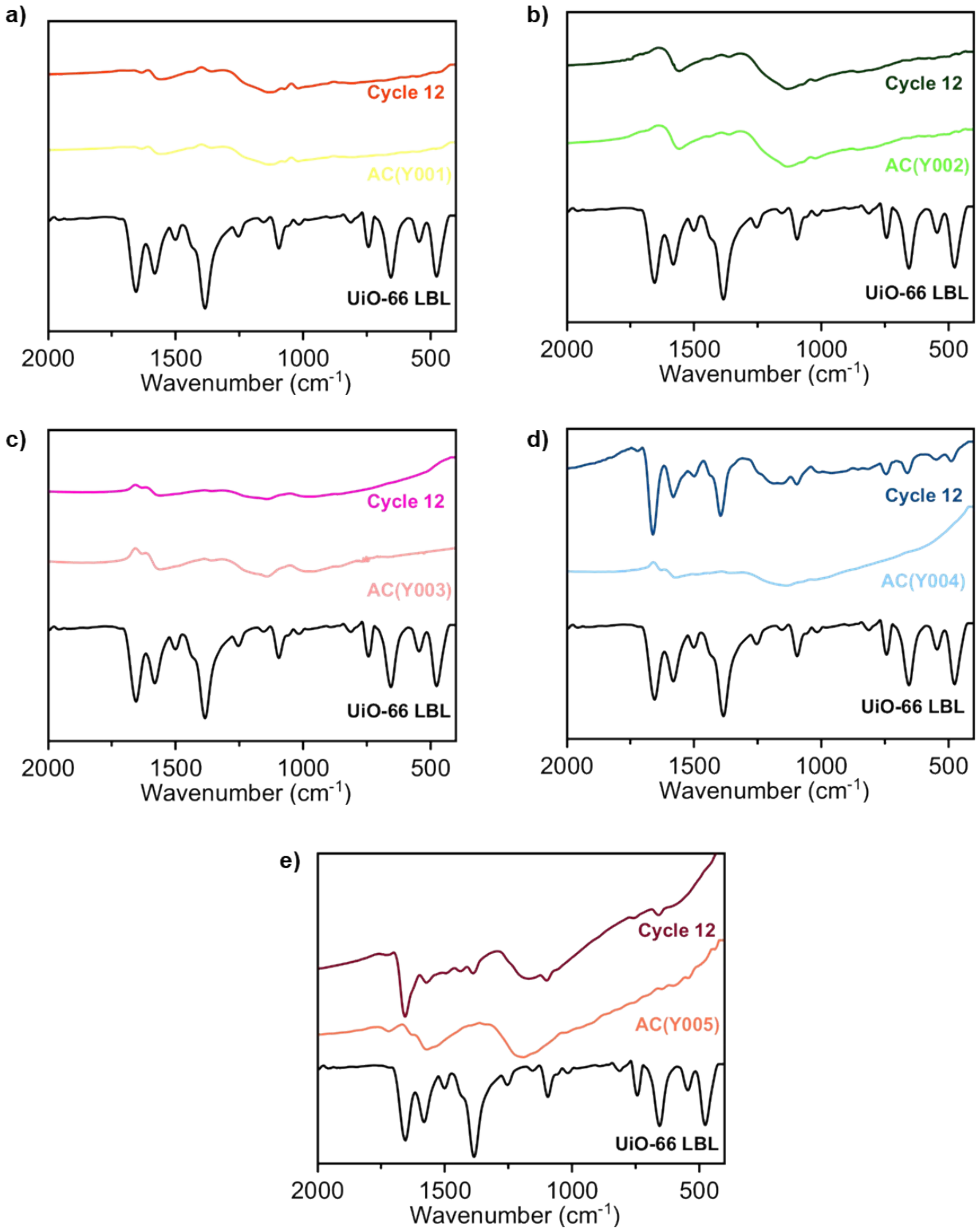

Figure S13. Fourier transformed infrared spectroscopy before and after layer-by-layer growth of UiO-66 thin films onto oxidized AC spheres: (a) AC(Y001), (b) AC(Y002), (c) AC(Y003), (d) AC(Y004) and (e) AC(Y005). Prior to measurements, all materials were vigorously washed with DMF and activated at 130ºC under vacuum during 6 hours.

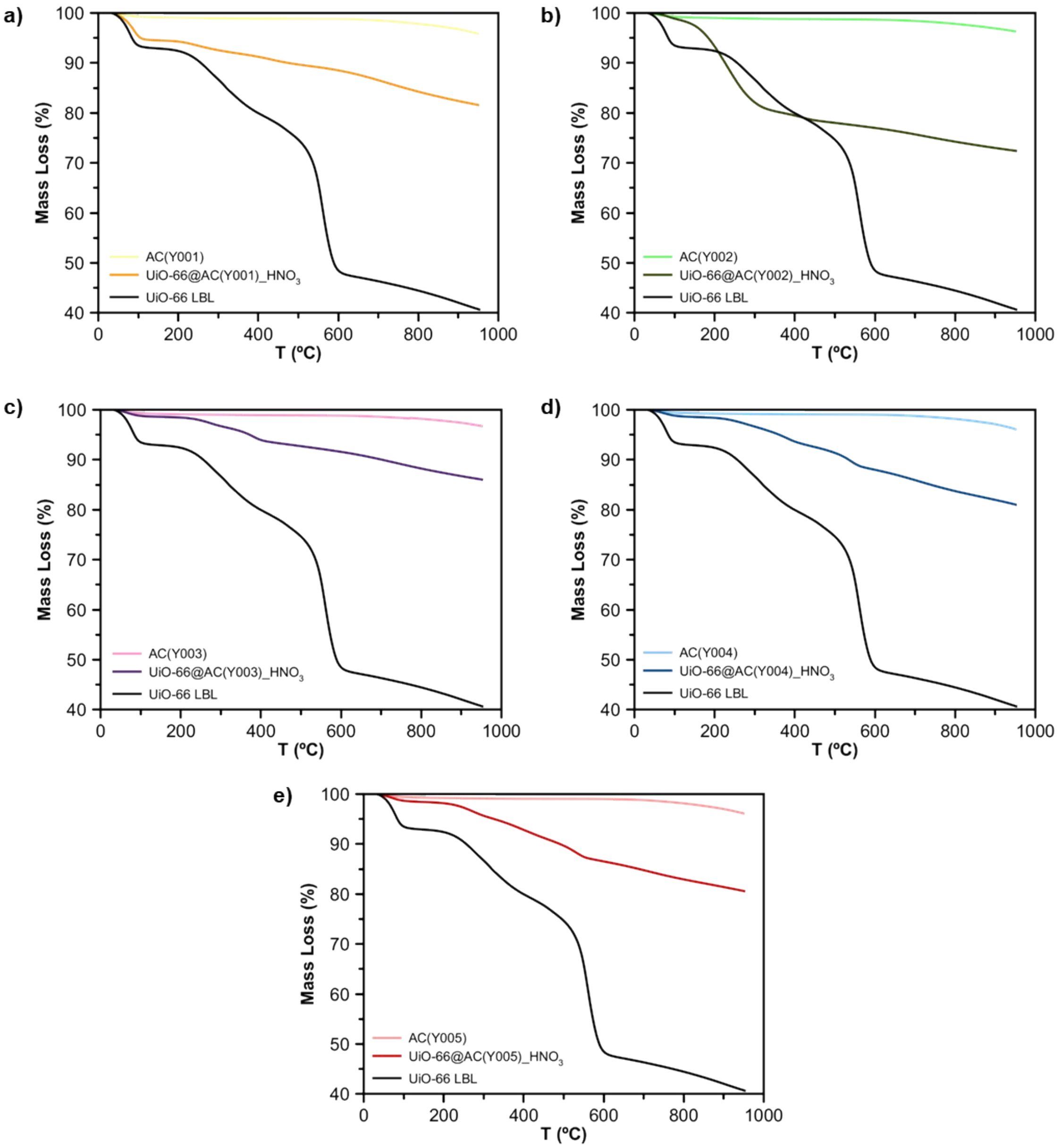

Figure S14. Thermogravimetric analysis before and after layer-by-layer growth of UiO-66 thin films onto oxidized AC spheres: (a) AC(Y001), (b) AC(Y002), (c) AC(Y003), (d) AC(Y004) and (e) AC(Y005).

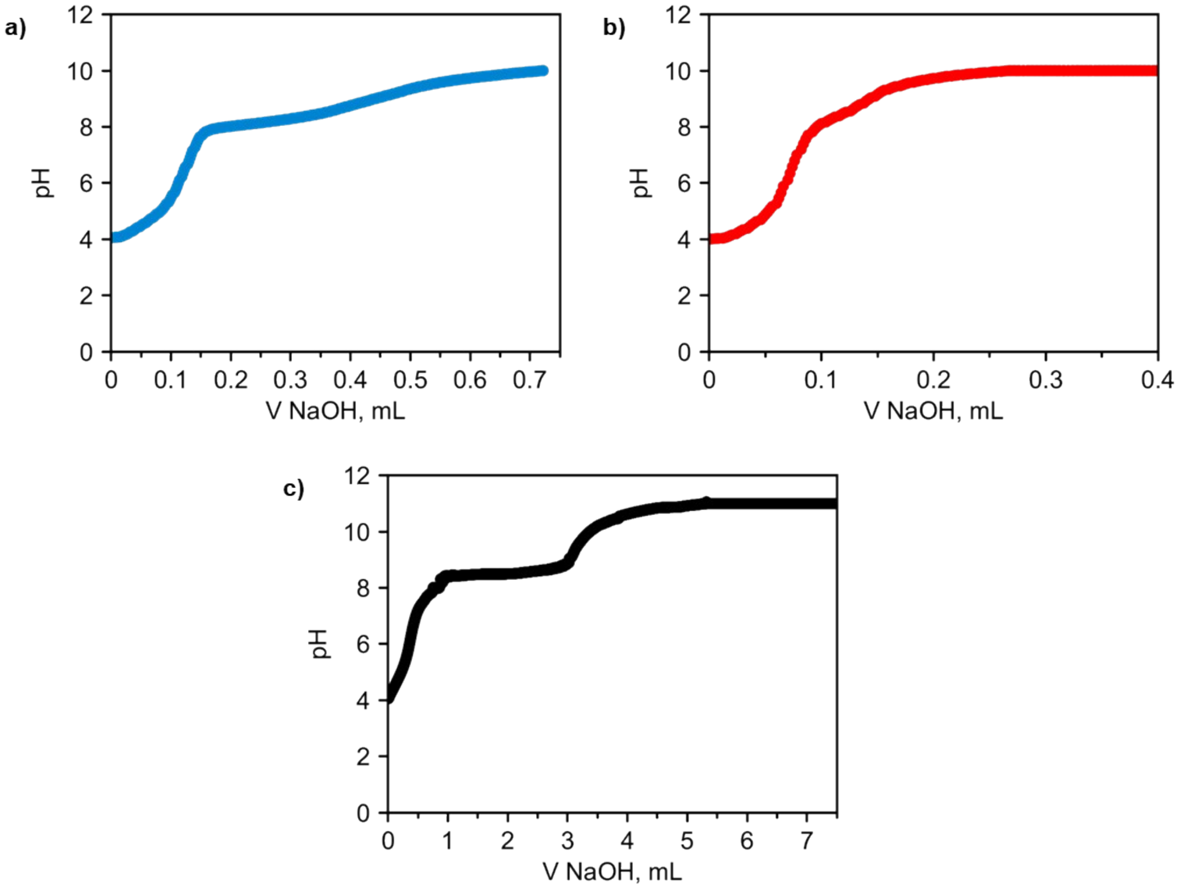

Figure S15. Acid-base titration curves for (a) UiO-66@AC(Y004)_HNO$_3$, (b) UiO-66@AC(Y005)_HNO$_3$ and (c) UiO-66 LBL.

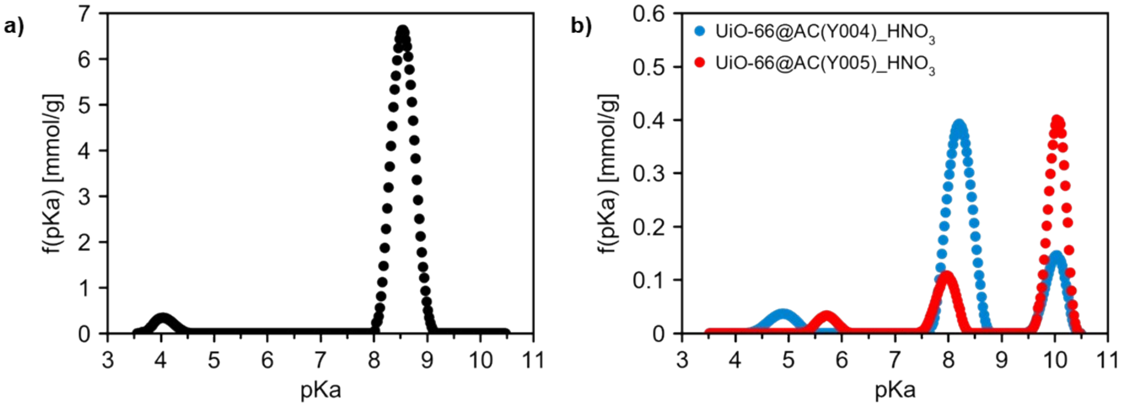

Figure S16. Distribution of acidity constants for (a) UiO-66 LBL and (b) UiO-66@AC(Y004-5)_HNO$_3$ composites.

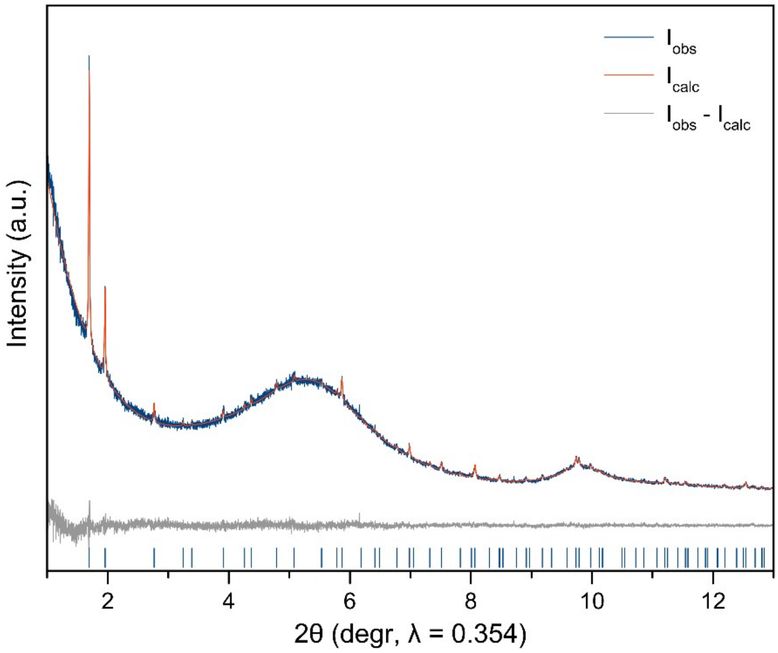

Figure S17. Graphical result of the whole powder pattern refinement carried out with the Le Bail method (R_p=0.018; R_{wp}=0.020) on the HR-PXRD pattern of as-synthesized UiO-66@AC(Y004) in terms of observed, calculated and difference traces (blue, red and grey, respectively). The positions of the Bragg reflection are indicated by blue ticks. Cell parameters: a=b=c= 20.7715(5) Å, V= 8962.0(7) Å^3.

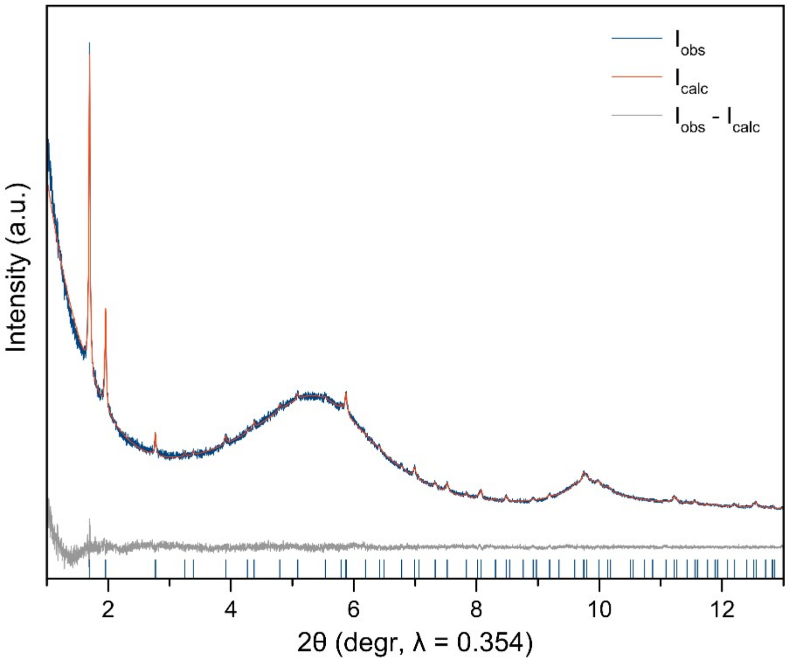

Figure S18. Graphical result of the whole powder pattern refinement carried out with the Le Bail method (R_p=0.019; R_{wp}=0.019) on the HR-PXRD pattern of as-synthesized UiO-66@AC(Y005) in terms of observed, calculated and difference traces (blue, red and grey, respectively). The positions of the Bragg reflection are indicated by blue ticks. Cell parameters: a=b=c 20.7481(7) Å, V= 8931 .8(9) Å^3.

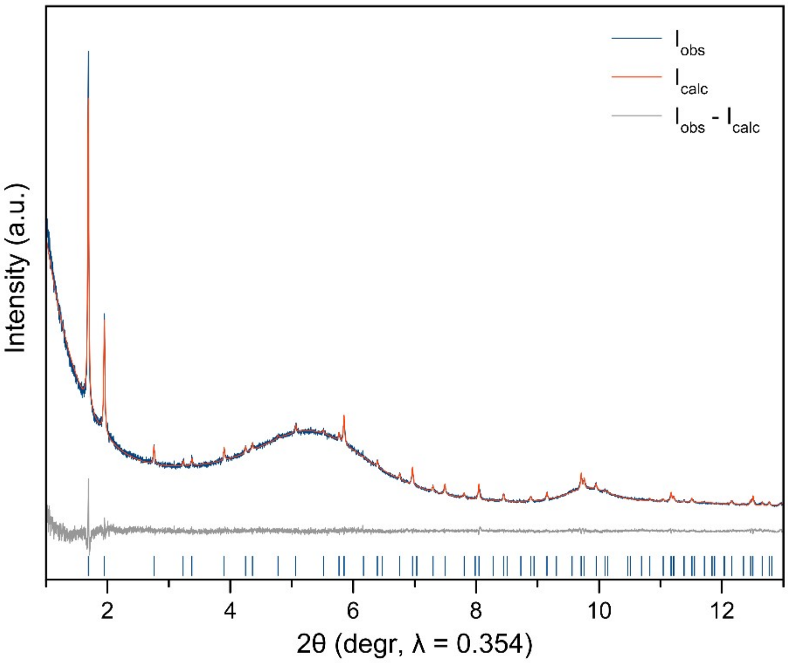

Figure S19. Graphical result of the whole powder pattern refinement carried out with the Le Bail method (R_p=0.022; R_{wp}=0.019) on the HR-PXRD pattern of as-synthesized UiO-66-NH_2@AC(Y004) in terms of observed, calculated and difference traces (blue, red and grey, respectively). The positions of the Bragg reflection are indicated by blue ticks. Cell parameters: a=b=c 20.8288 (3) Å, V= 9036. 4(3) Å^3.

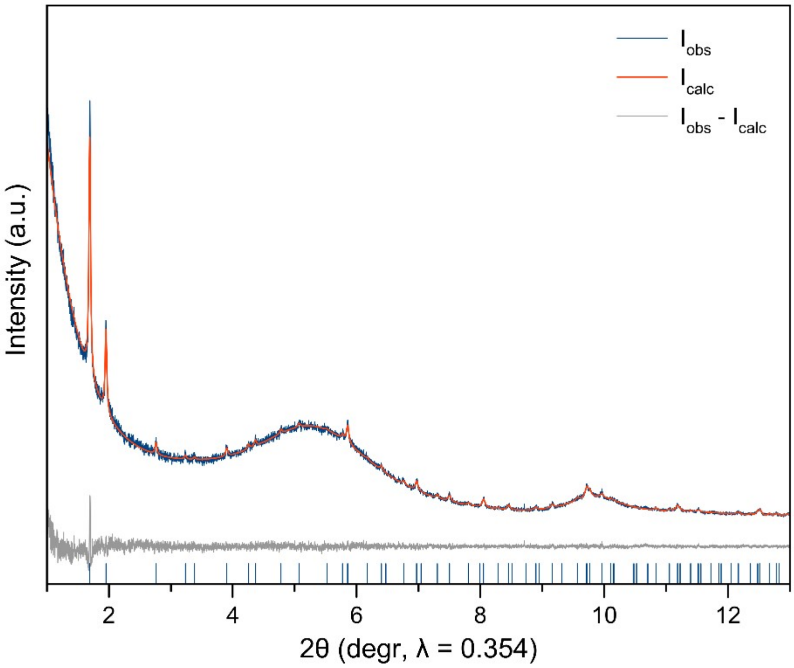

Figure S20. Graphical result of the whole powder pattern refinement carried out with the Le Bail method (R_p=0.026; R_{wp}=0.026) on the HR-PXRD pattern of as-synthesized UiO-66-NH_2@AC(Y005) in terms of observed, calculated and difference traces (blue, red and grey, respectively). The positions of the Bragg reflection are indicated by blue ticks. Cell parameters: a=b=c 20.8106 (8) Å, V= 9012.7(9) Å^3.

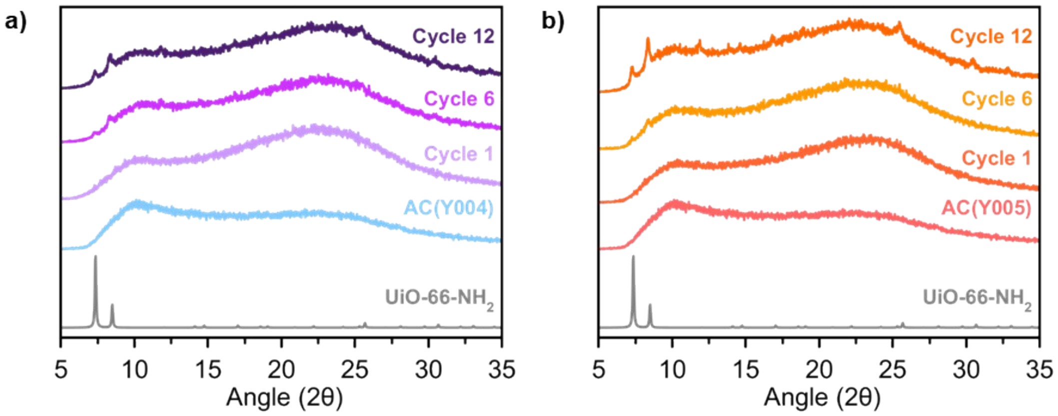

Figure S21. Follow-up of the layer-by-layer growth of UiO-66-NH$_2$ thin films on the oxidized activated carbon spheres (a) AC(Y004) and (b) AC(Y005) by powder X-ray diffraction. The simulated UiO-66-NH$_2$ pattern is shown in grey.

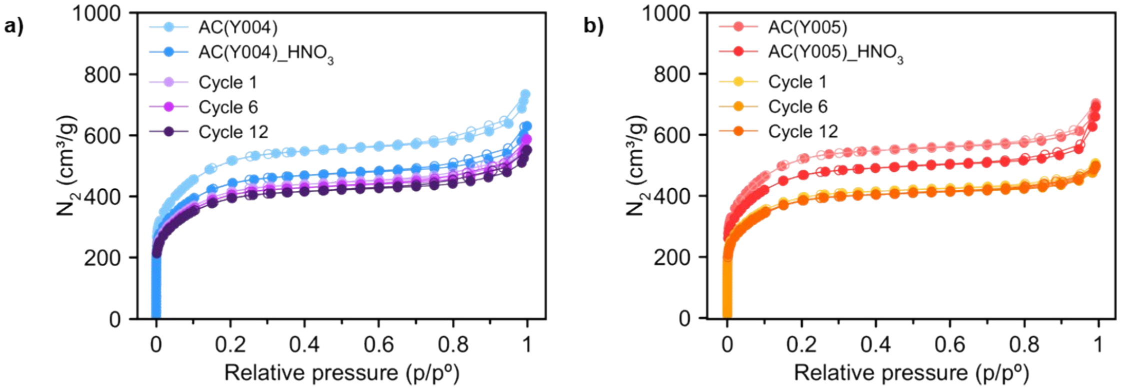

Figure S22. Follow-up of the layer-by-layer growth of UiO-66-NH$_2$ thin films on the oxidized activated carbon spheres (a) AC(Y004) and (b) AC(Y005) by nitrogen adsorption isotherms at 77K.

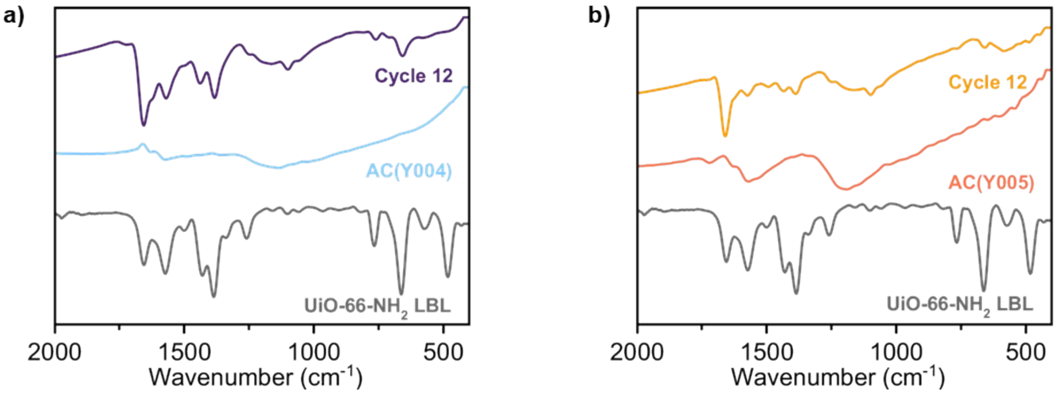

Figure S23. Fourier transformed infrared spectroscopy before and after layer-by-layer growth of UiO-66-NH$_2$ thin films onto oxidized AC spheres: (a) AC(Y004) and (b) AC(Y005). Prior to measurements, all materials were vigorously washed with DMF and activated at 130ºC under vacuum during 6 hours.

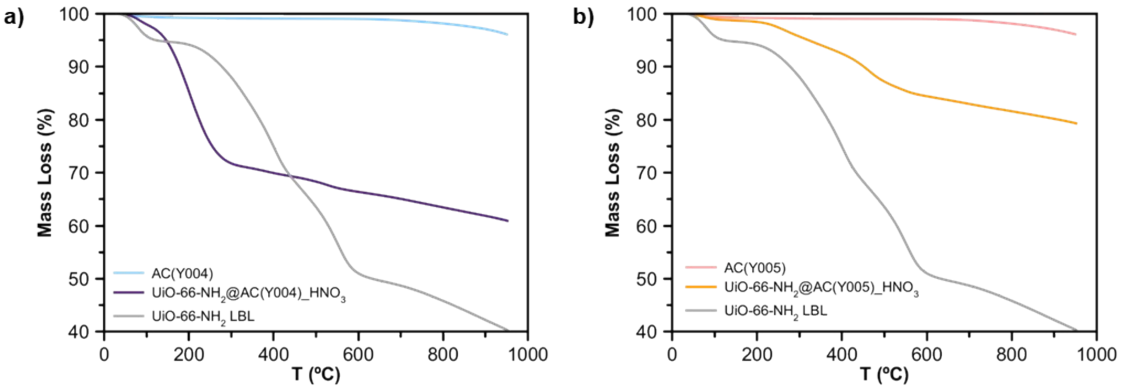

Figure S24. Thermogravimetric analysis before and after layer-by-layer growth of UiO-66-NH$_2$ thin films onto oxidized AC spheres: (a) AC(Y004), (b) AC(Y005).

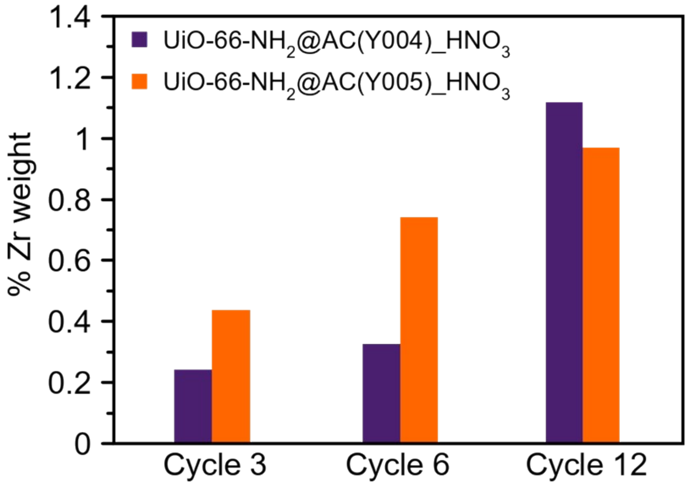

Figure S25. Follow-up of the layer-by-layer growth of UiO-66-NH$_2$ thin films on the activated carbon spheres by inductively coupled plasma – mass spectrometry.

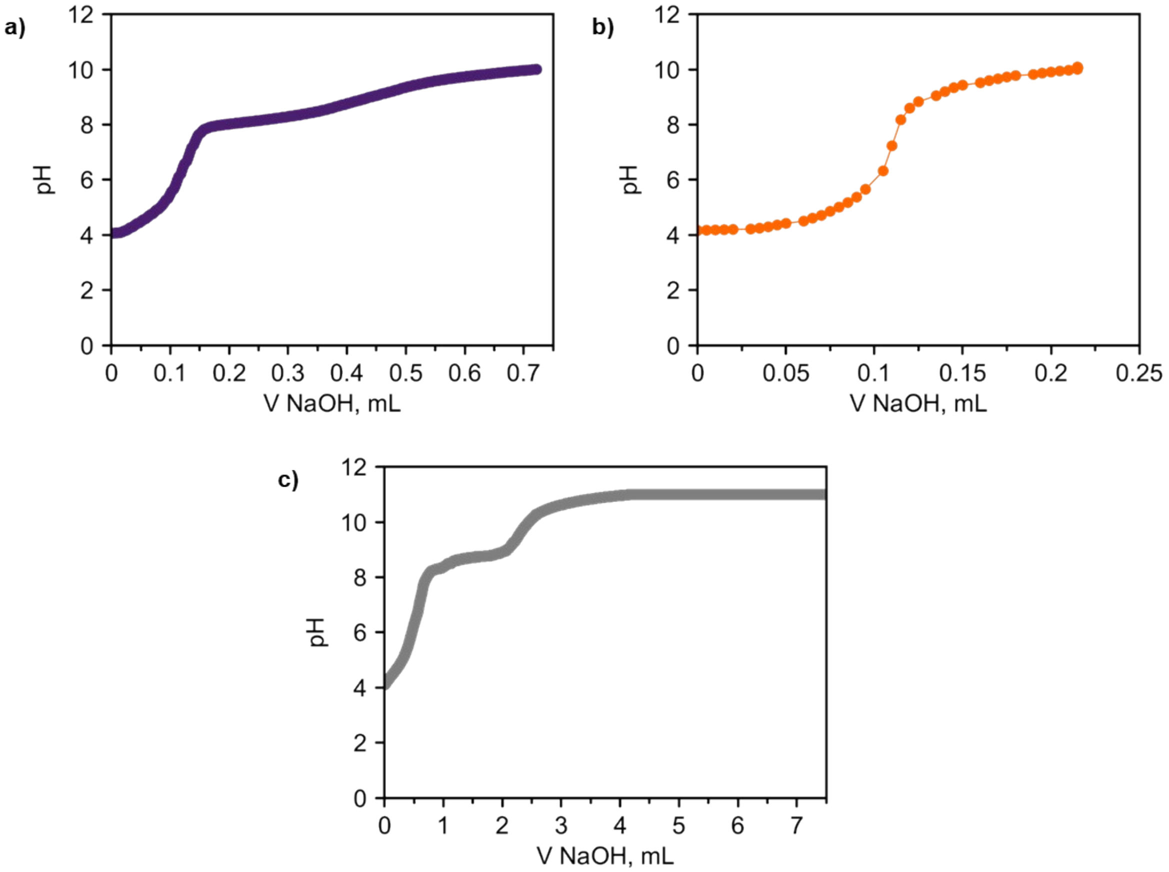

Figure S26. Acid-base titration curves for (a) UiO-66-NH_2@AC(Y004)_HNO_3, (b) UiO-66-NH_2@AC(Y005)_HNO_3 and (c) UiO-66-NH_2 LBL.

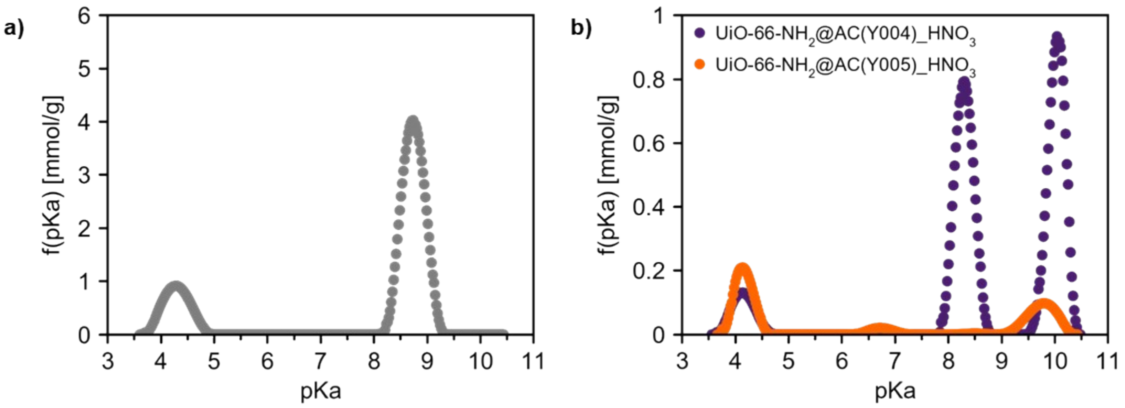

Figure S27. Distribution of acidity constants for (a) UiO-66-NH_2 LBL and (b) UiO-66-NH_2@AC(Y004-5)_HNO_3 composites.

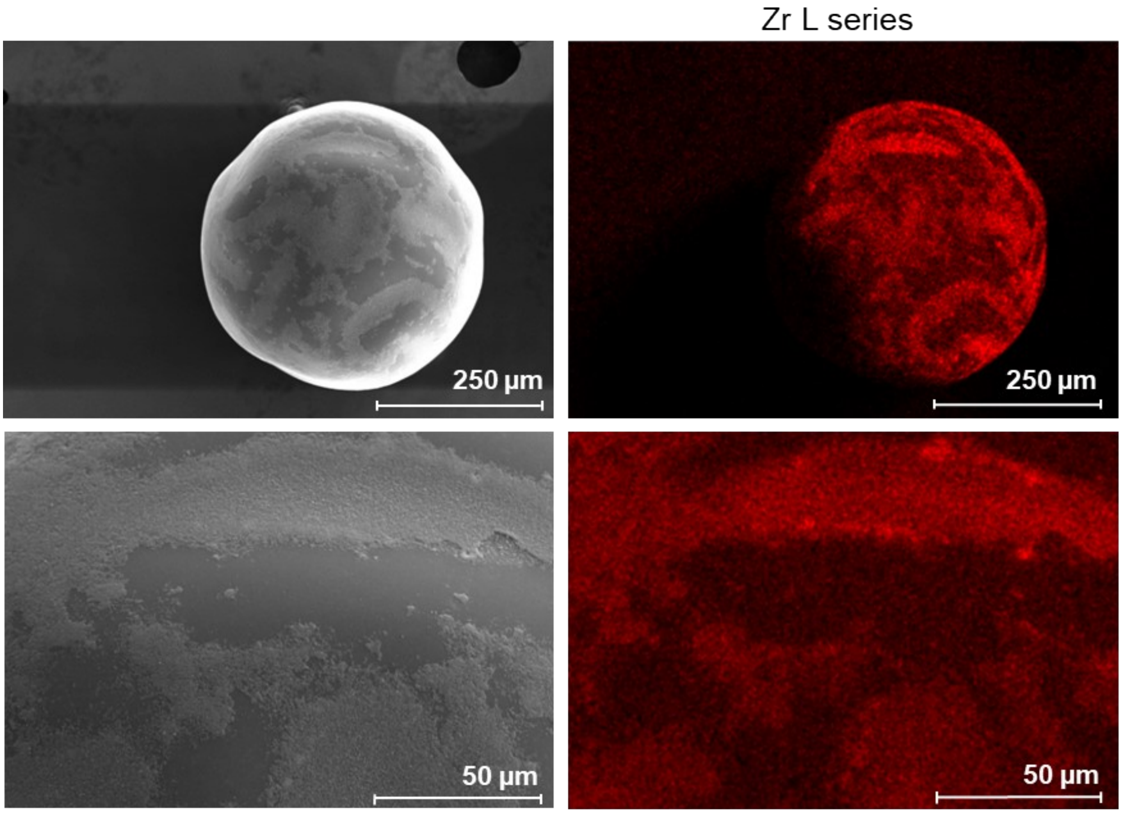

Figure S28. Scanning electron microscopy images and energy dispersive X-ray mapping for UiO-66@AC(Y004)_HNO_3.

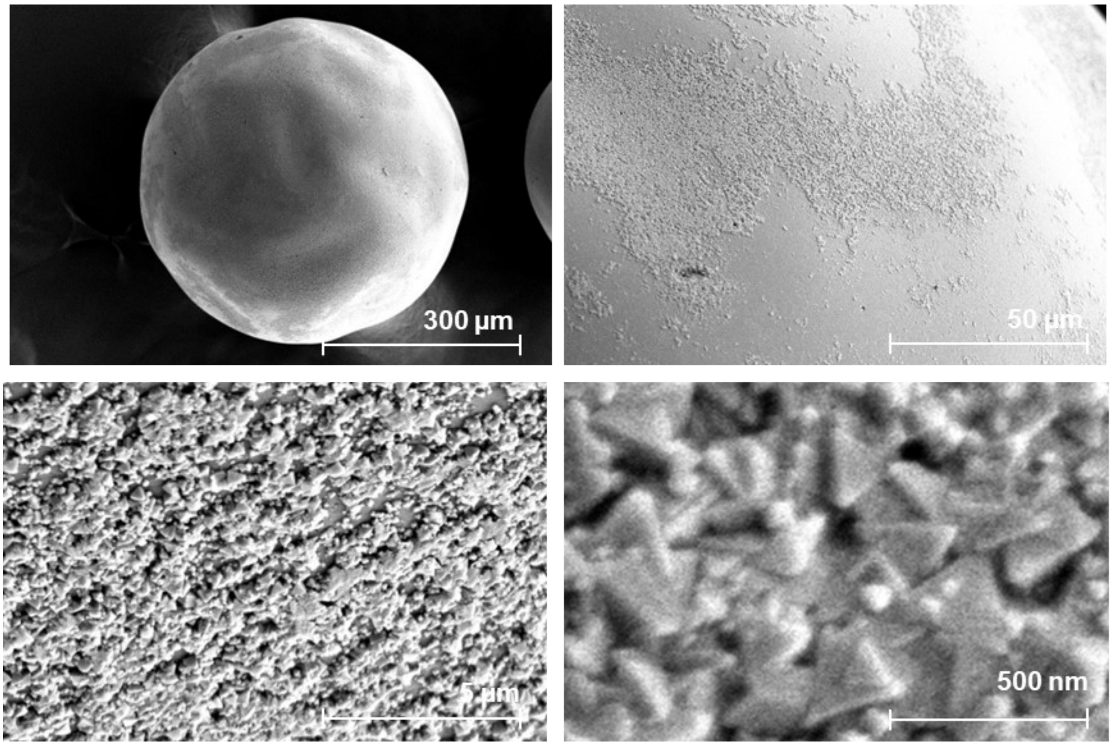

Figure S29. Scanning electron microscopy images for UiO-66@AC(Y005)_HNO_3.

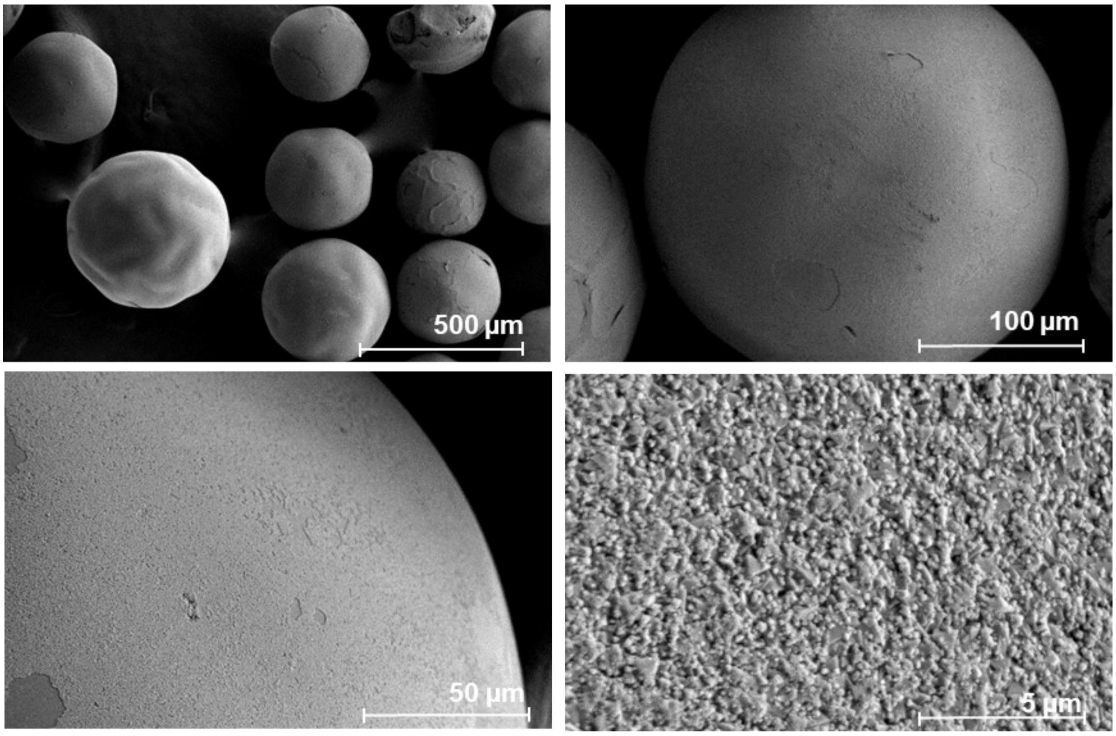

Figure S30. Scanning electron microscopy images for UiO-66-NH_2@AC(Y004)_HNO_3.

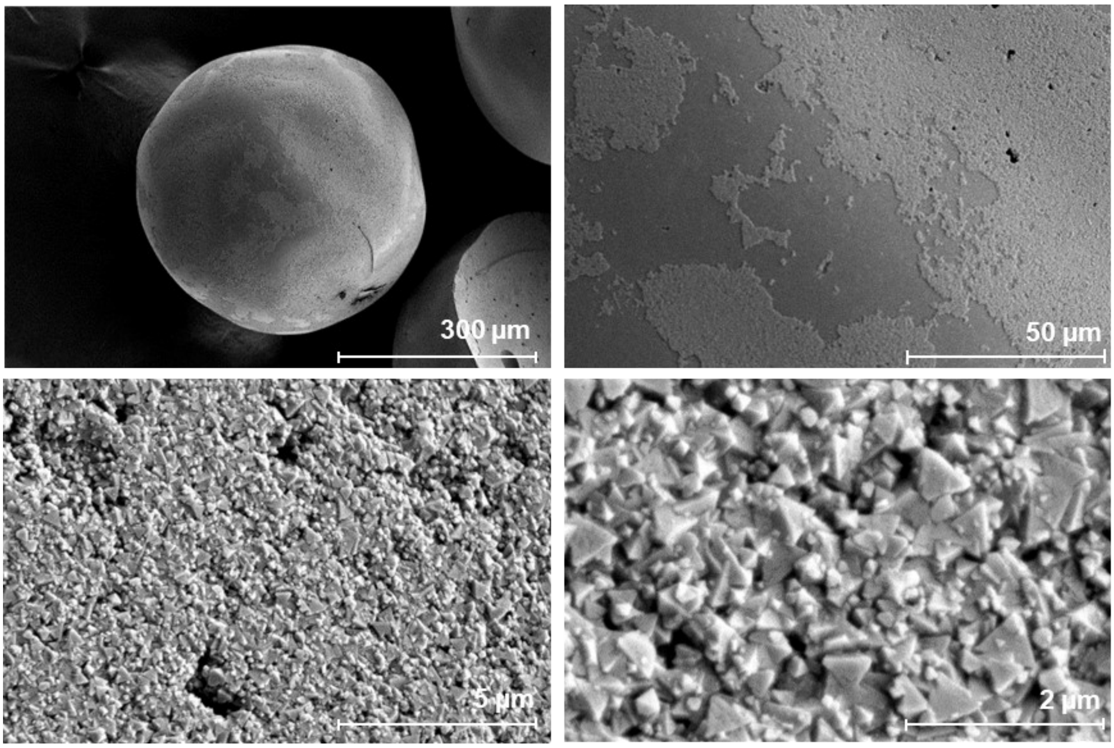

Figure S31. Scanning electron microscopy images for UiO-66-NH_2@AC(Y005)_HNO_3.

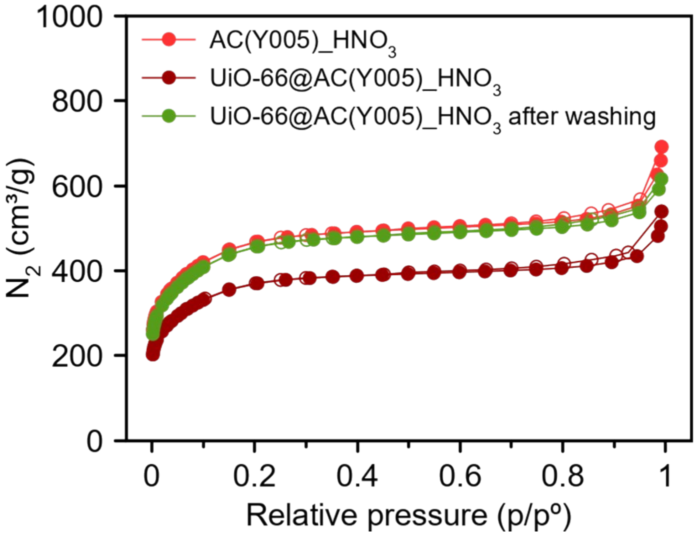

Figure S32. Nitrogen adsorption isotherms at 77 K of AC(Y005)_HNO$_3$ and UiO-66@AC(Y005)_HNO$_3$ before and after vigorous wash. Conditions of washing step: UiO-66@AC(Y005)_HNO$_3$ composite was washed with DMF at reflux during 15 minutes.

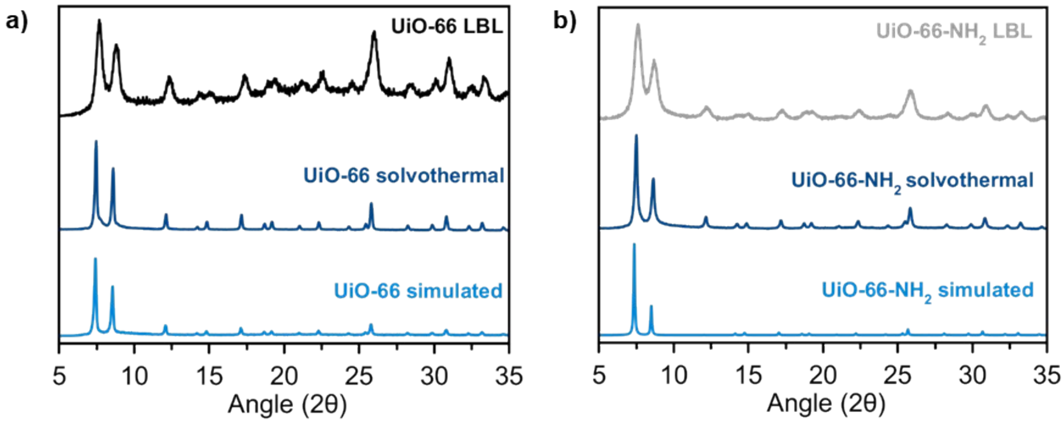

Figure S33. Powder X-Ray Diffraction patterns of synthesized (LBL and solvothermal types) (a) UiO-66 and (b) UiO-66-NH$_2$.

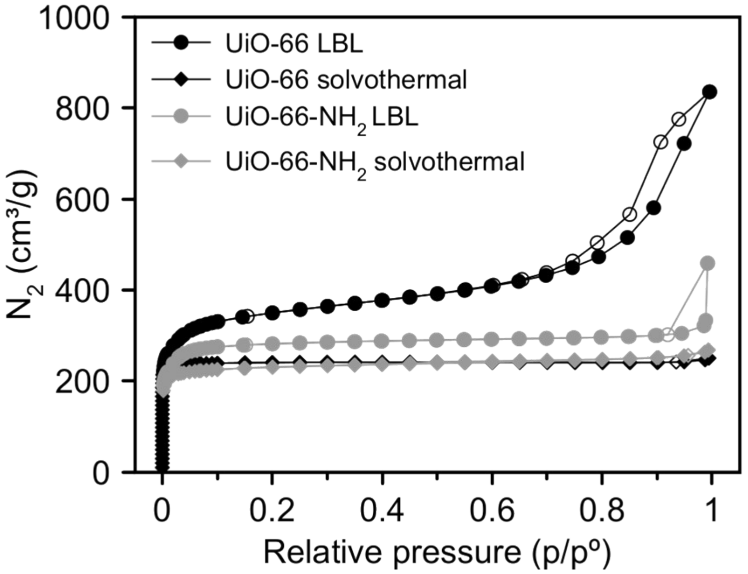

Figure S34. Nitrogen adsorption isotherms at 77 K of UiO-66(-NH_2) materials after solvothermal and LBL synthesis. BET (UiO-66 LBL) = 1,155 m^2/g, BET (UiO-66 solvothermal) = 970 m^2/g, BET (UiO-66-NH_2 LBL) = 910 m^2/g and BET (UiO-66-NH_2 solvothermal) = 909 m^2/g.

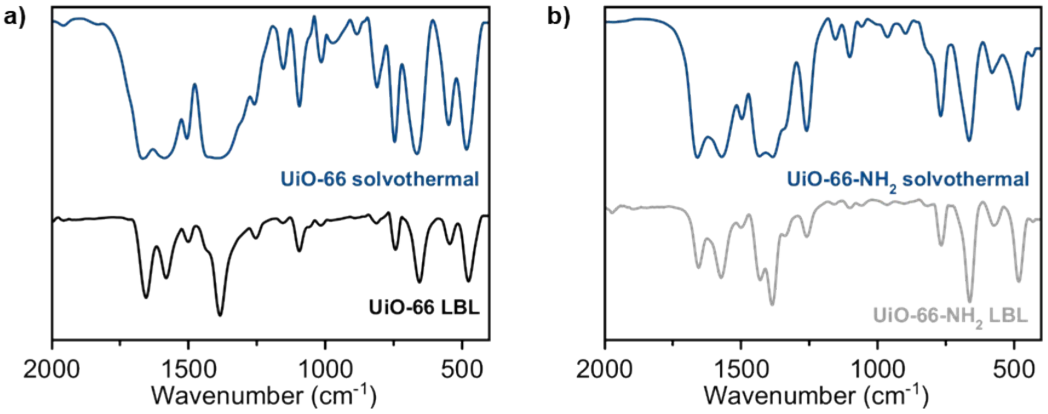

Figure S35. Fourier transformed infrared spectroscopy of synthesized (a) UiO-66 and (b) UiO-66-NH_2 (LBL and solvothermal types).

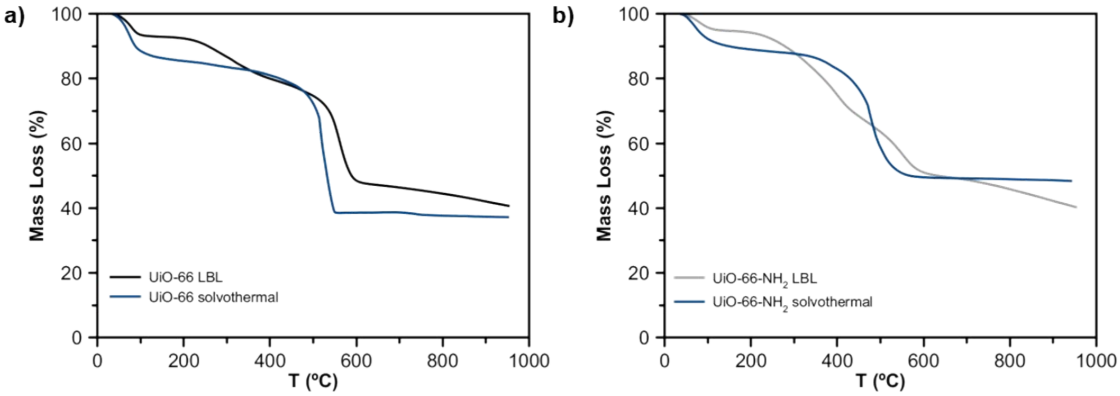

Figure 36. Thermogravimetric analysis of solvothermal and LBL type (a) UiO-66 and (b) UiO-66-NH_2.

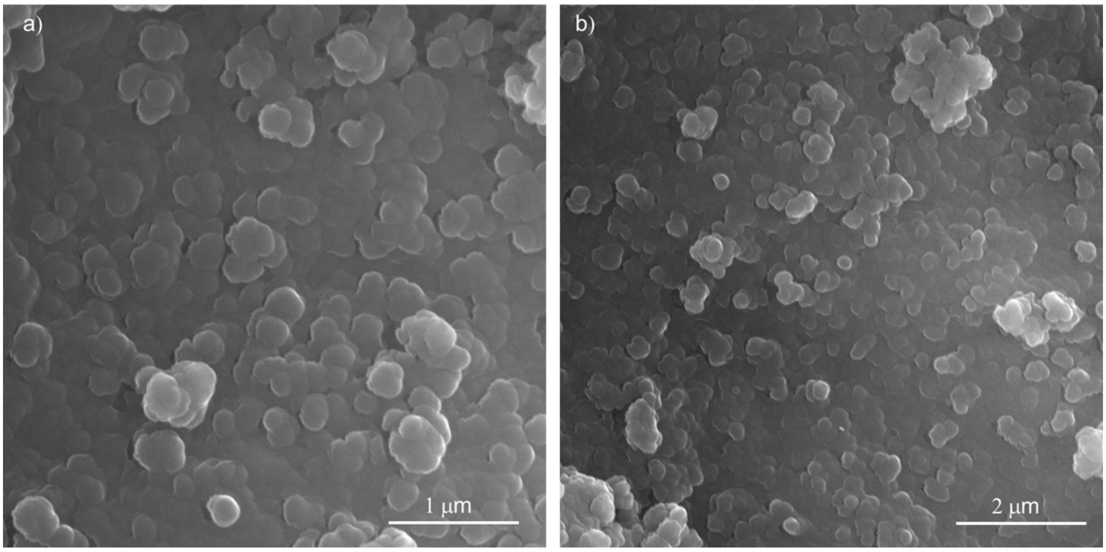

Figure S37. Scanning electron microscopy images for UiO-66 LBL (a) and UiO-66-NH_2 LBL (b).

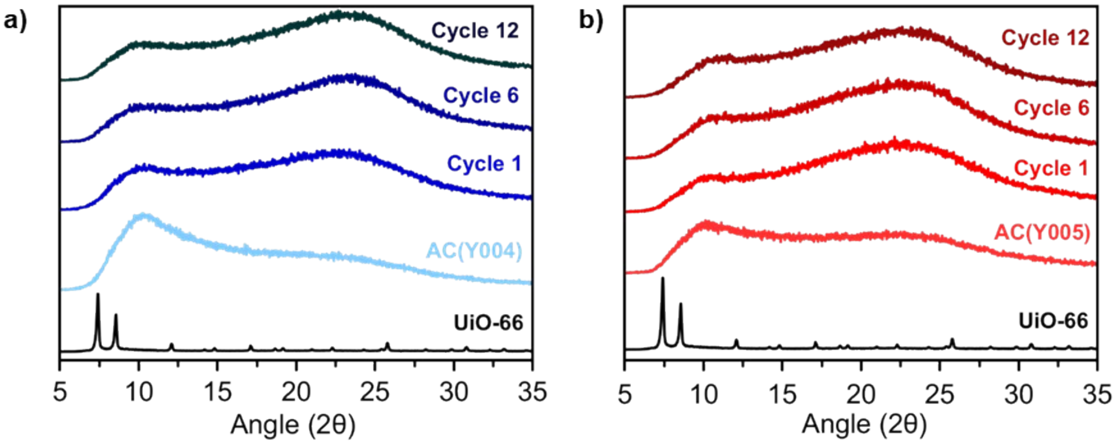

Figure S38. Follow-up of the layer-by-layer growth of UiO-66 thin films on the non-oxidized activated carbon spheres (a) AC(Y004) and (b) AC(Y005) by powder X-ray diffraction. The simulated UiO-66 pattern is shown in black.

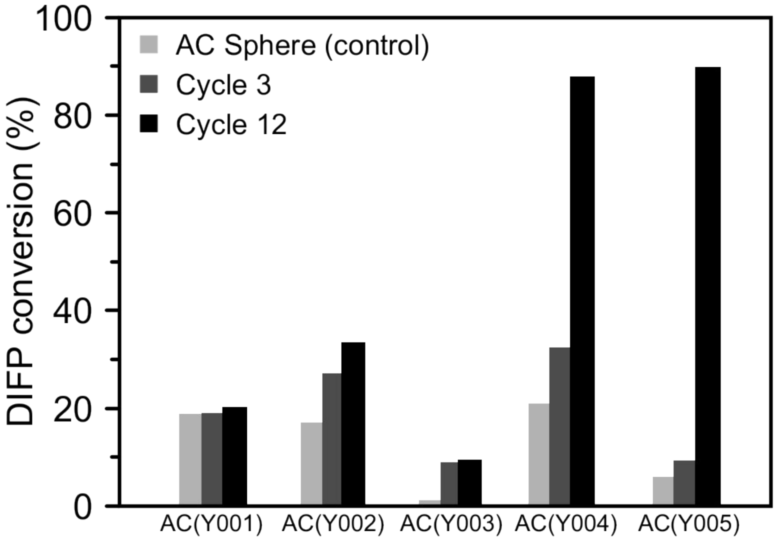

Figure S39. Comparison of DIFP degradation by different activated carbon spheres non-oxidized (control) and UiO-66@AC(Y00n)_HNO_3 (n = 1-5) composites at different cycles after 24 h.

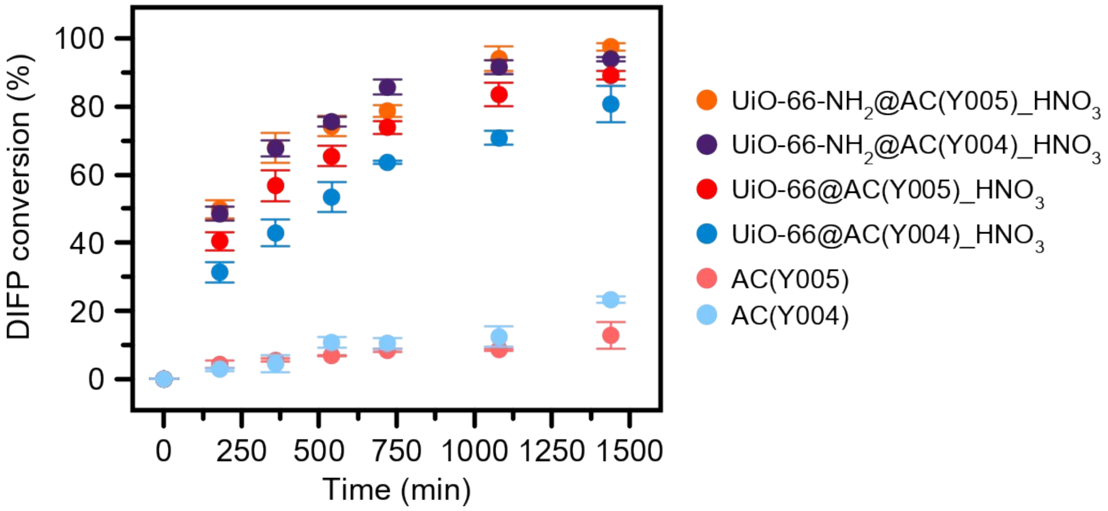

Figure S40. Evolution of DIFP hydrolysis by pristine AC(Y00n) spheres and UiO-66(NH_2)@AC(Y00n)_HNO_3 composites (n=4, 5) against time.

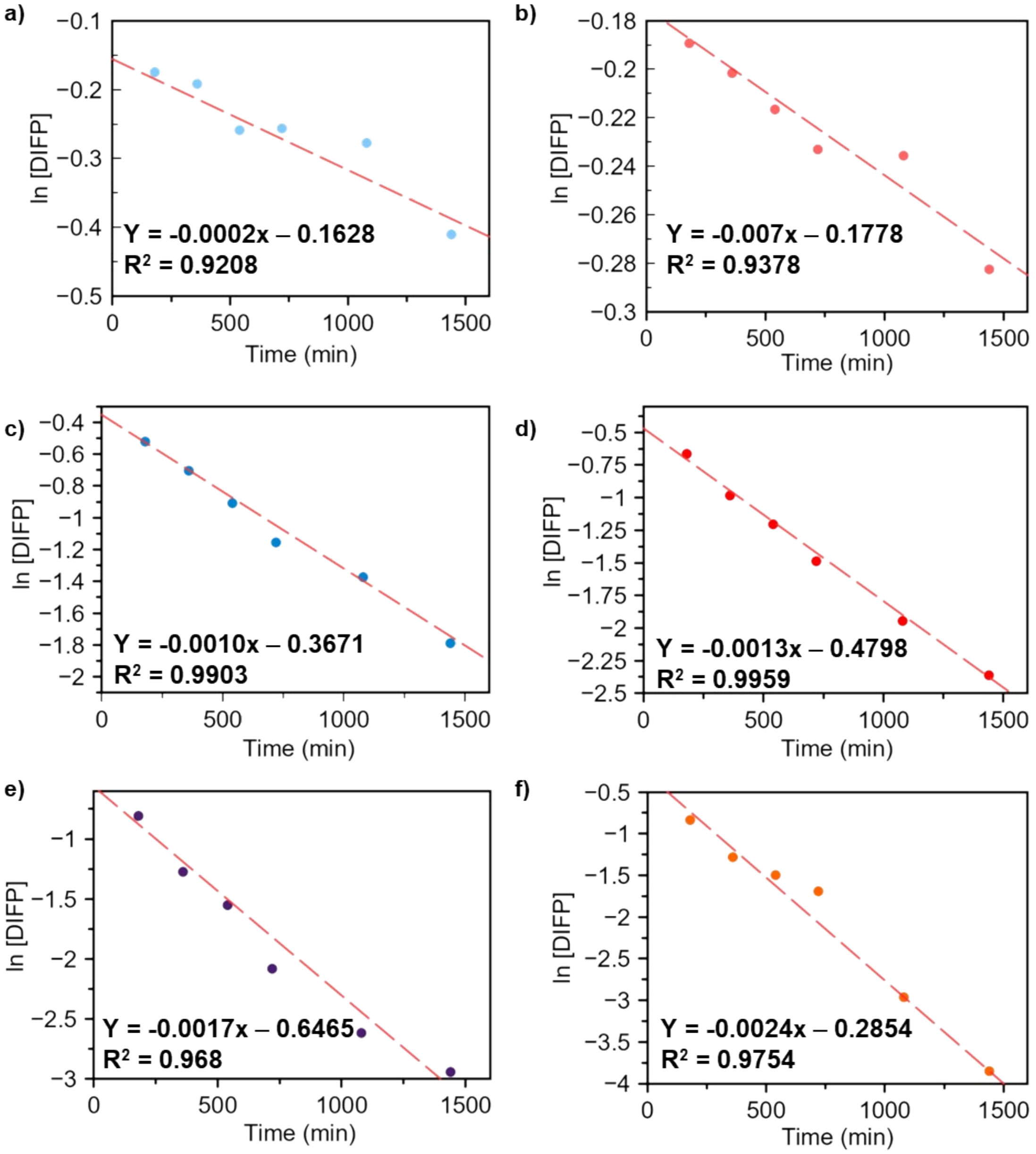

Figure S41. Fitting curves to first-order kinetic model of DIFP hydrolytic degradation by (a) AC(Y004), (b) AC(Y005), (c) UiO-66@AC(Y004) _HNO_3, (d) UiO-66@AC(Y005) _HNO_3, (e) UiO-66-NH_2@AC(Y004) _HNO_3 and (f) UiO-66-NH_2@AC(Y005) _HNO_3.

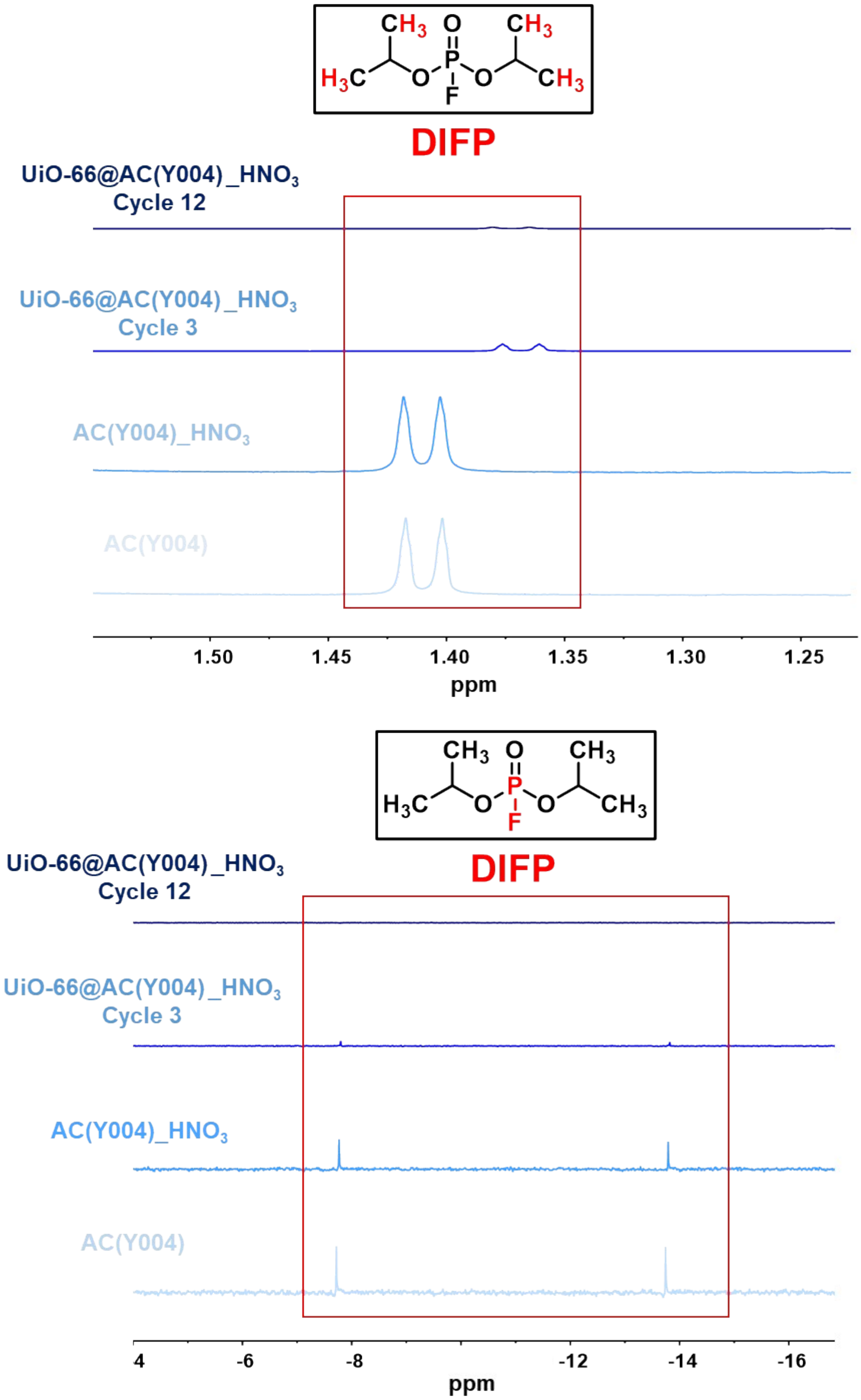

Figure S42. ^{1}H NMR (top) and ^{31}P NMR (bottom) spectra of diisopropylfluorophosphate (DIFP) by AC(Y004) and UiO-66@AC(Y004) _HNO$_3$ based materials in CDCl$_3$.

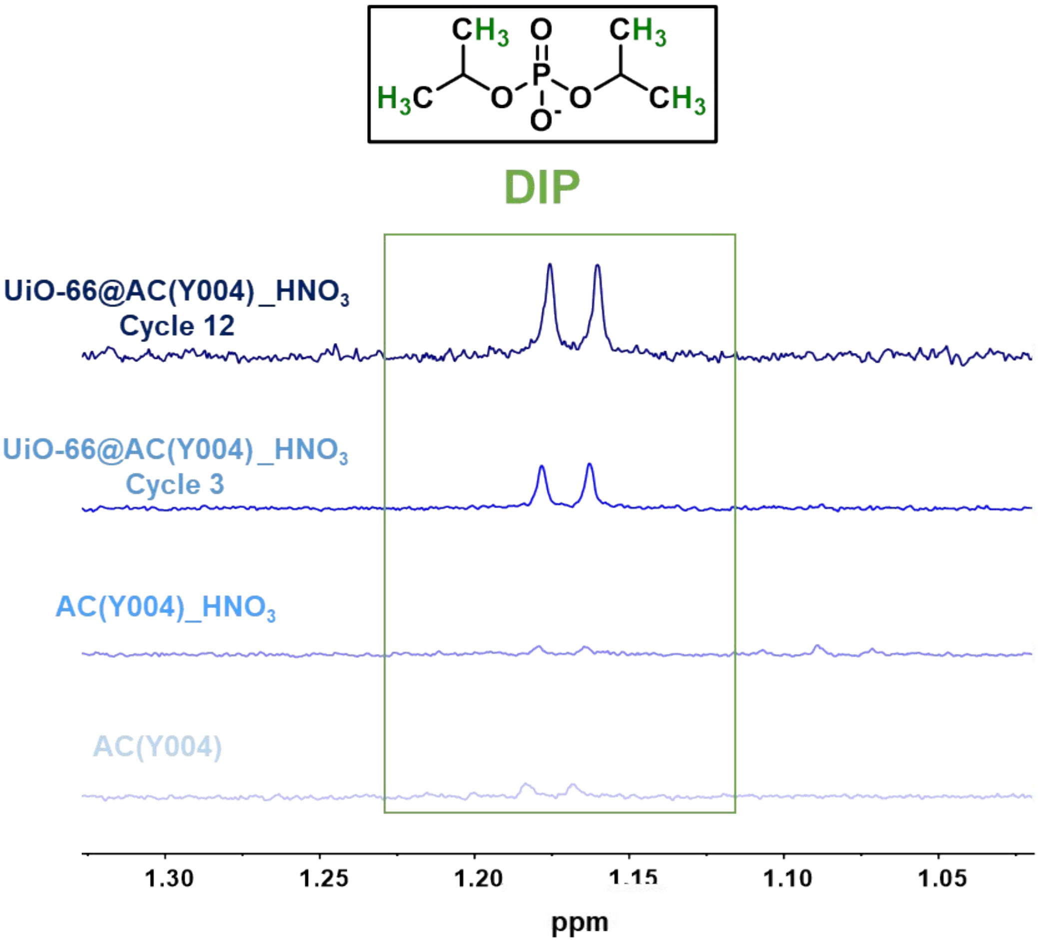

Figure S43. ^{1}H NMR spectra of hydrolysis product (DIP) by AC(Y004) and UiO-66@AC(Y004) _HNO$_3$ based materials in D$_2$O.

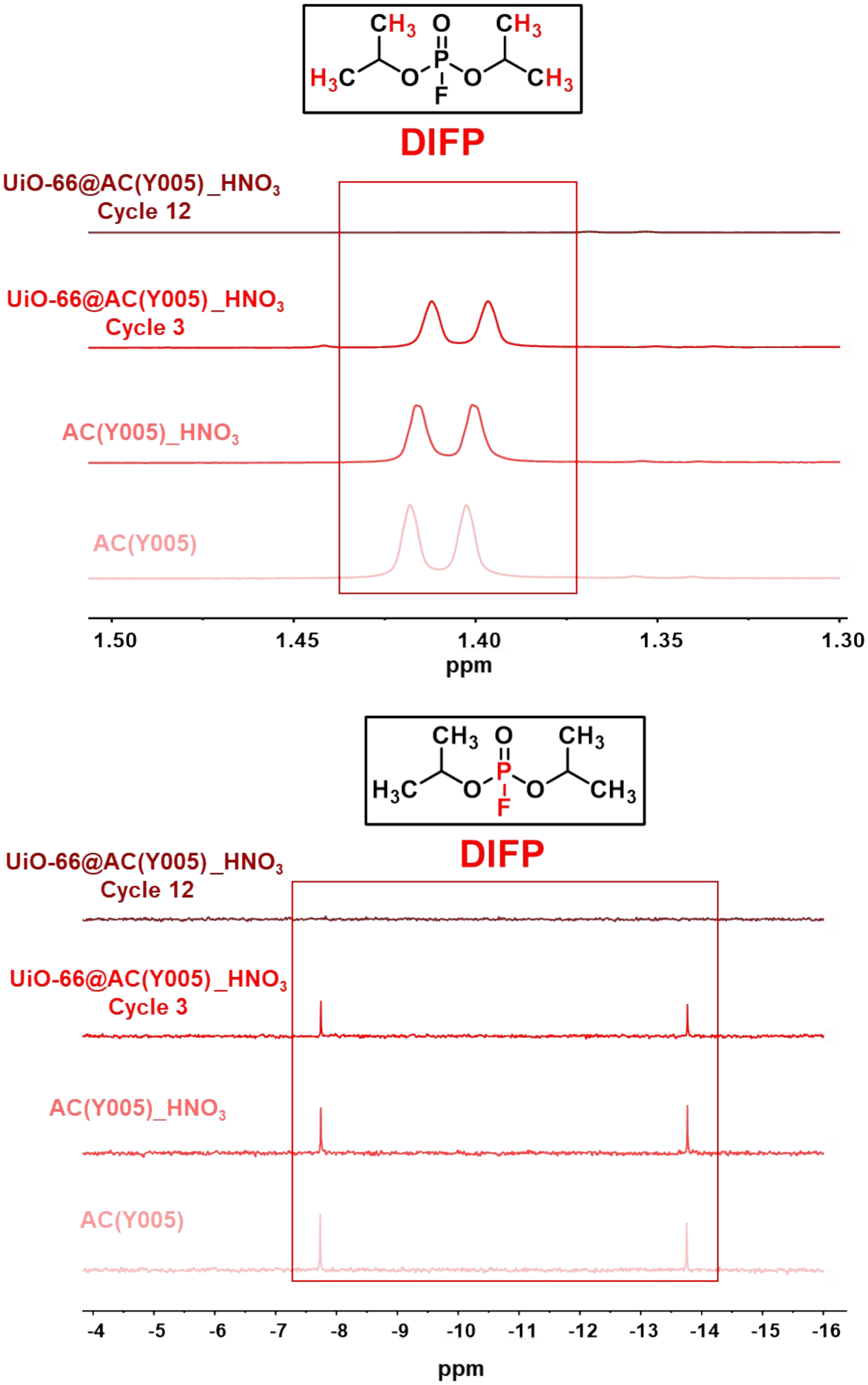

Figure S44. ^{1}H NMR (top) and ^{31}P NMR (bottom) spectra of diisopropylfluorophosphate (DIFP) by AC(Y005) and UiO-66@AC(Y005) _HNO_3 based materials in $CDCl_3$.

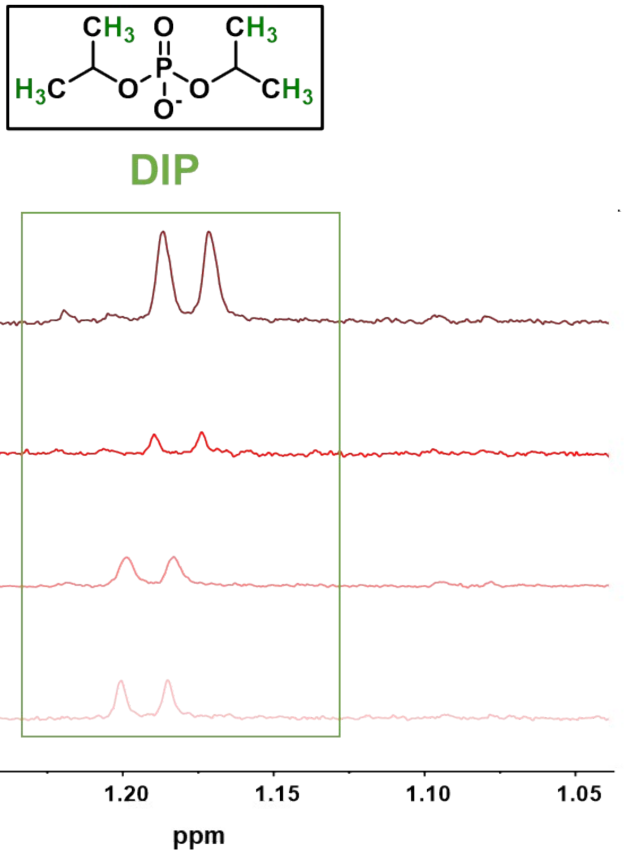

Figure S45. ^{1}H NMR spectra of hydrolysis product (DIP) by AC(Y005) and UiO-66@AC(Y005) _HNO_3 based materials in D_2O.

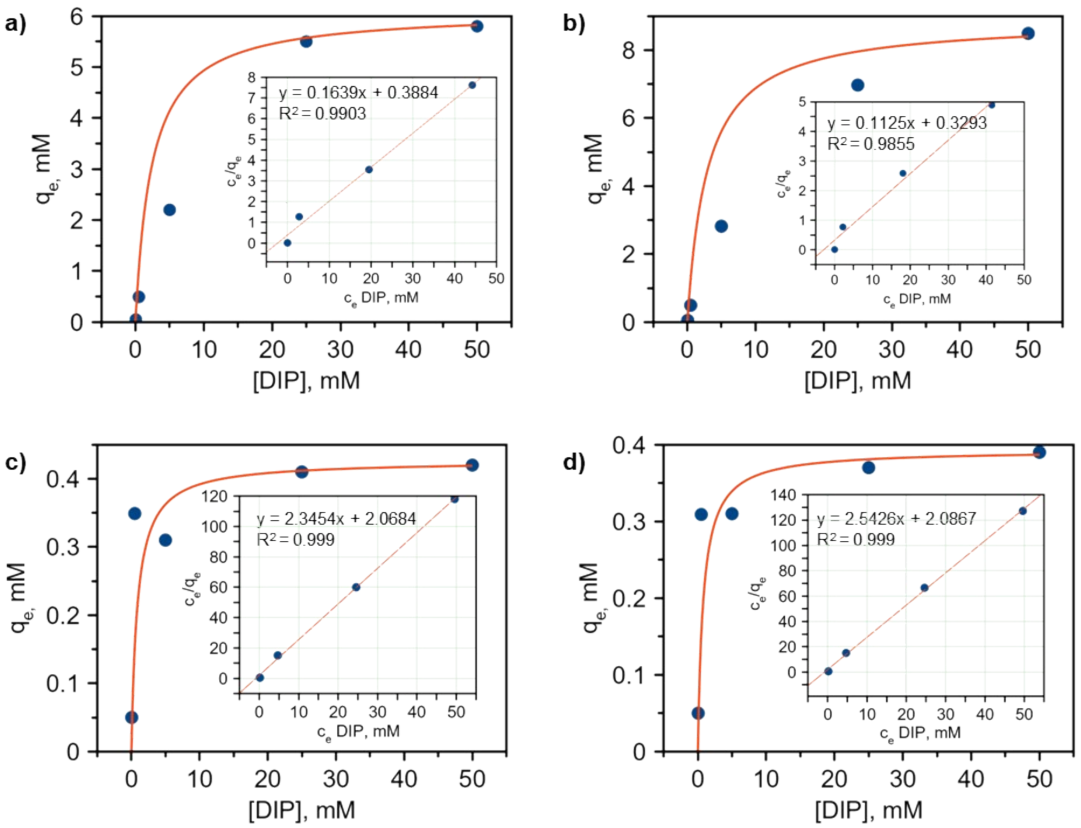

Figure S46. Solid-liquid adsorption isotherms of DIP (293 K) by (a) AC(Y004)_HNO$_3$, (b) AC(Y005)_HNO$_3$, (c) UiO-66 LBL and (d) UiO-66-NH$_2$ LBL materials. Inset shows the linear fitting to Langmuir model.

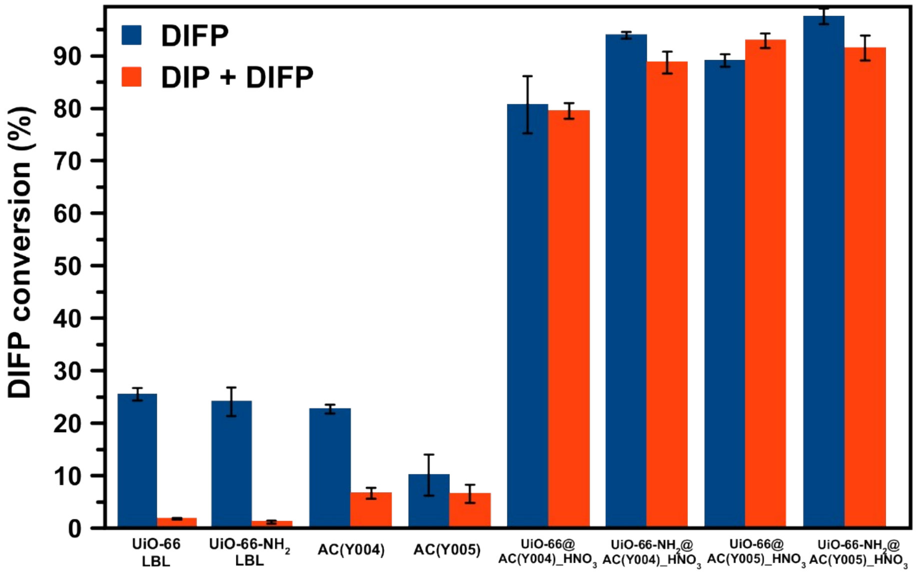

Figure S47. Comparison of the inhibitory effect of DIP in DIFP hydrolytic degradation after 24 hours by UiO-66(-NH$_2$) LBL, AC(Y00n) and UiO-66(-NH$_2$)@AC(Y00n)_HNO$_3$ (n=4,5) materials: original DIFP degradation (blue) and DIFP degradation after previous inhibition with DIP (red).

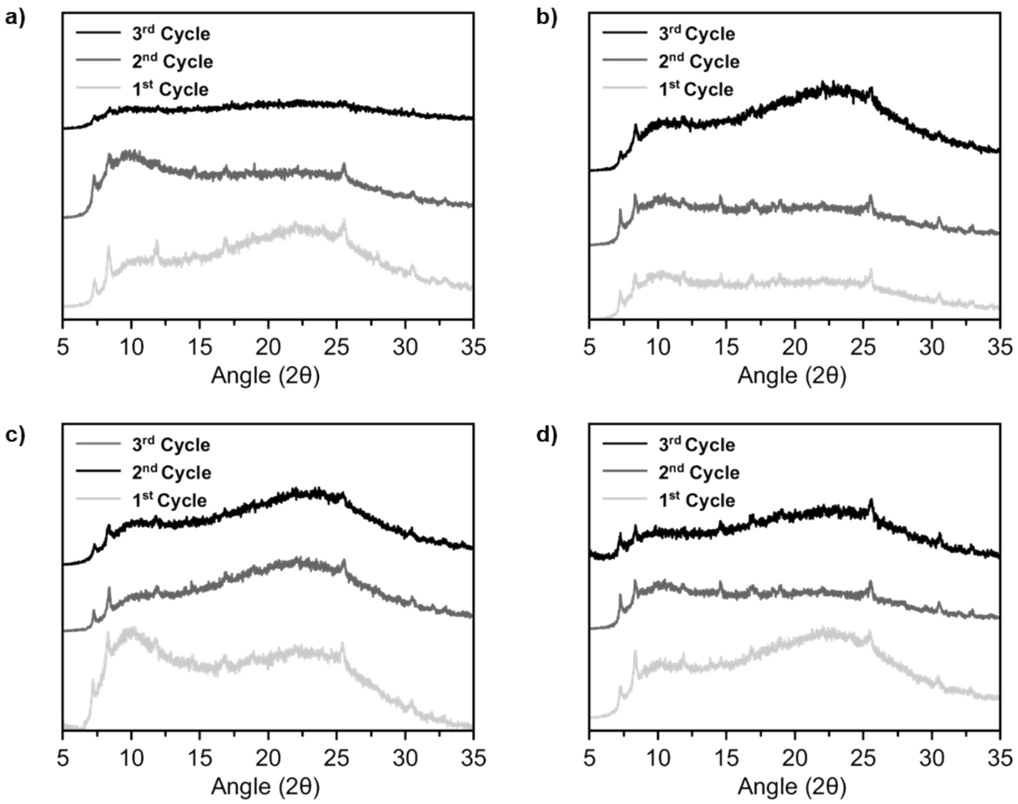

Figure S48. Evaluation by Powder X-Ray diffraction of the integrity of the catalyst after each recyclability test of DIFP degradation (a) UiO-66@AC(Y004) _HNO_3, (b) UiO-66@AC(Y005) _HNO_3, (c) UiO-66-NH_2@AC(Y004) _HNO_3 and (d) UiO-66-NH_2@AC(Y005) _HNO_3.

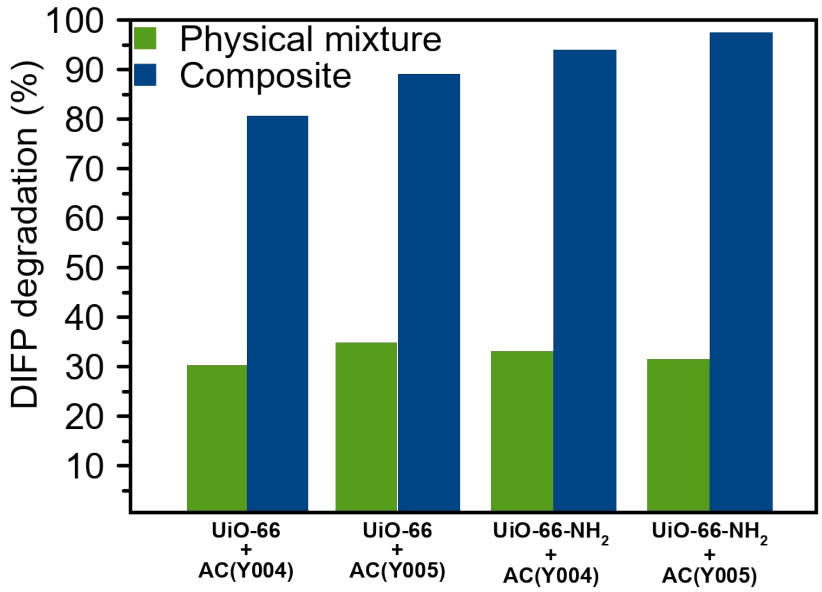

Figure S49. Comparison of DIFP hydrolytic degradation after 24 hours by UiO-66(-NH_2)@AC(Y00n) (n = 4.5) composites (blue) and their physical mixture (green).

Tables

Table S1. BET surface area (m^2/g) of AC(Y005) spheres oxidized with H_2O_2, HNO_3 and $(NH_4)_2S_2O_8$ (and subsequently treated with urea or thiourea).

Sample	H_2O_2	HNO_3	$(NH_4)_2S_2O_8$
AC(Y005)	1,661	1,555	1,458
AC(Y005) (urea)	1,342	1,216	1,389
AC(Y005) (thiourea)	858	988	1,081

Table S2. BET surface area (m^2/g) of AC(Y00n)_HNO_3 and UiO-66@AC(Y00n)_HNO_3 (n = 1-5) materials throughout each impregnation cycle.

Sample	AC(Y001)	AC(Y002)	AC(Y003)	AC(Y004)	AC(Y005)
AC_oxidized	1,100	765	1,181	1,483	1,555
Cycle 1	952	818	1,056	1,423	1,341
Cycle 6	962	724	1,051	1,401	1,348
Cycle 12	990	688	1,040	1,374	1,242

Table S3. Final concentration of Zr obtained by ICP-MS and UiO-66(-NH_2) proportion of each Zr-MOF@AC_HNO_3 composite.

Materials	% Zr	% MOF
UiO-66@AC(Y001)_HNO_3	0.034	0.101
UiO-66@AC(Y002)_HNO_3	0.015	0.045
UiO-66@AC(Y003)_HNO_3	0.072	0.215
UiO-66@AC(Y004)_HNO_3	1.332	3.962
UiO-66@AC(Y005)_HNO_3	0.349	1.038
UiO-66-NH_2@AC(Y004)_HNO_3	1.115	3.318
UiO-66-NH_2@AC(Y005)_HNO_3	0.967	2.877

Table S4. BET surface area (m^2/g) of UiO-66-NH_2@AC(Y00n)_HNO_3 (n = 4, 5) composites throughout each impregnation cycle.

Sample	AC(Y004)	AC(Y005)
HNO_3 oxidized	1,483	1,555
Cycle 1	1,399	1,324
Cycle 6	1,366	1,299
Cycle 12	1,322	1,293

Table S5. pKa values and the amount of groups in mmol/g (below pKa values) obtained by software *Saieus_pK* from acid-base titration curves.

Sample	Initial pH	4-5	5-6	6-7	7-8	8-9	9-11	Total [mmol/g]
AC(Y001)	7.63	-	5.03 0.210	-	-	8.65 0.050	9.80 0.005	0.265
AC(Y002)	8.48	4.60 0.030		6.18 0.200	-	-	-	0.230
AC(Y003)	6.36	-	5.09 0.114	-	-	8.06 0.045	9.72 0.050	0.210
AC(Y004)	7.19	-	-	6.05 0.055	-	8.40 0.080	9.92 0.074	0.200
AC(Y005)	8.28	-	5.65 0.030	-	-	8.05 0.058	9.90 0.068	0.166
AC(Y001)_HNO$_3$	4.80	4.55 0.224	-	6.20 0.012	7.62 0.032	-	10.13 0.130	0.398
AC(Y002)_HNO$_3$	4.40	4.90 0.089	-	6.21 0.025	-	8.14 0.071	10.11 0.050	0.235
AC(Y003)_HNO$_3$	4.27	4.90 0.089	-	6.30 0.022	-	8.14 0.075	10.02 0.050	0.236
AC(Y004)_HNO$_3$	3.52	4.91 0.089	-	6.30 0.025	-	8.18 0.045	10.11 0.050	0.209
AC(Y005)_HNO$_3$	3.74	3.89 0.238	-	6.16 0.041	-	-	10.08 0.214	0.487
UiO-66@ AC(Y004) _HNO$_3$	5.63	4.84 0.023	-	-	-	8.25 0.0225	10.14 0.90	0.338
UiO-66-NH$_2$@ AC(Y004) _HNO$_3$	5.44	4.2 0.072	-	-	-	8.30 0.364	10.10 0.390	0.824
UiO-66@ AC(Y005) _HNO$_3$	5.58	-	5.74 0.015	-	7.93 0.050	-	10.1 0.163	0.228
UiO-66-NH$_2$@ AC(Y005) _HNO$_3$	5.34	4.06 0.095	-	6.87 0.012	-	-	9.81 0.070	0.177
UiO-66 LBL	4.24	4.02 0.157	-	-	-	8.57 3.56	-	3.72
UiO-66-NH$_2$ LBL	4.69	4.3 0.609	-	-	-	8.79 2.27		2.879

Table S6. Kinetic parameters of the catalytic hydrolysis of DIFP by MOF@AC_HNO$_3$ Spheres.

Sample	Rate Constant (min^{-1})	Half-time (h)	Maximum Hydrolysis (%)
UiO-66@AC(Y004)_HNO$_3$	0.059	7.8	80.7
UiO-66@AC(Y005) _HNO$_3$	0.0013	4.5	89.1
UiO-66-NH$_2$@AC(Y004)_HNO$_3$	0.097	1.8	93.9
UiO-66-NH$_2$@AC(Y005)_HNO$_3$	0.127	3.8	96.5

Table S7. α partition coefficients of DIP for the AC sphere/MOF interphase calculated for a spheres:MOF 1:1 ratio and calculated values taking into account the sphere:MOF ratio found in the composites.

Interphase	α partition coefficient	
	AC:MOF (1:1)	**AC_MOF composite**
AC(Y004)_HNO_3 /UiO-66	0.377	9.52
AC(Y005)_HNO_3 /UiO-66	0.307	29.5
AC(Y004)_HNO_3 / UiO-66-NH2	0.342	11.4
AC(Y004)_HNO_3 /UiO-66-NH2	0.280	9.33

Table S8. % DIFP degradation by UiO-66(-NH_2)@AC(Y00n)_HNO_3 (n=4,5) composites throughout each catalytic cycle.

Materials	**1st cycle**	**2nd cycle**	**3rd cycle**
UiO-66@AC(Y004)_HNO_3	80.7	66.2	52.0
UiO-66@AC(Y005)_HNO_3	89.1	78.5	78.0
UiO-66-NH_2@AC(Y004)_HNO_3	93.9	80.0	75.9
UiO-66-NH_2@AC(Y005)_HNO_3	96.5	78.9	77.8

References.

[1] DeStefano, M. R.; Islamoglu, T.; Garibay, S. J.; Hupp, J. T.; Farha, O. K. Room-Temperature Synthesis of UiO-66 and Thermal Modulation of Densities of Defect Sites. Chem. Mater. 2017, 29 (3), 1357–1361. https://doi.org/10.1021/acs.chemmater.6b05115.

[2] Gil-San-Millan, R.; López-Maya, E.; Platero-Prats, A. E.; Torres-Pérez, V.; Delgado, P.; Augustyniak, A. W.; Kim, M. K.; Lee, H. W.; Ryu, S. G.; Navarro, J. A. R. Magnesium Exchanged Zirconium Metal–Organic Frameworks with Improved Detoxification Properties of Nerve Agents. J. Am. Chem. Soc. 2019, 141 (30), 11801– 11805. https://doi.org/10.1021/jacs.9b05571.

[3] Gil-San-Millan, R.; López-Maya, E.; Hall, M.; Padial, N. M.; Peterson, G. W.; DeCoste, J. B.; Rodríguez-Albelo, L. M.; Oltra, J. E.; Barea, E.; Navarro, J. A. R. Chemical Warfare Agents Detoxification Properties of Zirconium Metal–Organic Frameworks by Synergistic Incorporation of Nucleophilic and Basic Sites. ACS Appl. Mater. Interfaces 2017, 9 (28), 23967–23973. https://doi.org/10.1021/acsami.7b06341.

[4] Gil-San-Millan, R.; Delgado, P.; Lopez-Maya, E.; Martin-Romera, J. D.; Barea, E.; Navarro, J. A. R. Layer-by-Layer Integration of Zirconium Metal-Organic Frameworks onto Activated Carbon Spheres and Fabrics with Model Nerve Agent Detoxification Properties. ACS Applied Materials and Interfaces 2021, 13 (42), 50491–50496. https://doi.org/10.1021/acsami.1c12095.